CANCER

A live single-cell reporter assay links intratumor heterogeneity to metastatic proclivity in Ewing sarcoma

Tugba Keskin[1], Beatrice Rucci[1], Sandrine Cornaz-Buros[1], Patricia Martin[1], Carlo Fusco[1], Liliane Broye[1], Katarina Cisarova[2], Elizabeth M. Perez[3,4,5], Igor Letovanec[6,7], Stefano La Rosa[7], Stephane Cherix[8], Manuel Diezi[9], Raffaele Renella[9], Paolo Provero[10], Mario L. Suvà[3,4], Ivan Stamenkovic[1]*†, Nicolò Riggi[1†]

Targeting of the most aggressive tumor cell subpopulations is key for effective management of most solid malignancies. However, the metastable nature of tumor heterogeneity, which allows cells to transition between strong and weak tumorigenic phenotypes, and the lack of reliable markers of tumor-promoting properties hamper identification of the most relevant cells. To overcome these obstacles, we designed a functional microRNA (miR)–based live-cell reporter assay to identify highly tumorigenic cells in xenotransplants of primary Ewing sarcoma (EwS) 3D cultures. Leveraging the inverse relationship between cell pluripotency and miR-145 expression, we successfully separated highly tumorigenic, metastasis-prone (miR-145^{low}) cells from poorly tumorigenic, non-metastatic (miR-145^{high}) counterparts. Gene expression and functional studies of the two cell populations identified the EPHB2 receptor as a prognostic biomarker in patients with EwS and a major promoter of metastasis. Our study provides a simple and powerful means to identify and isolate tumor cells that display aggressive behavior.

INTRODUCTION

One of the greatest challenges to cancer therapy is the effective targeting of cells that provide the driving force to the growth and progression of any given tumor. Despite the long-standing notion that solid tumors are heterogeneous, most of the conventional cytotoxic drug–based strategies, which still dominate anticancer treatment, do not account for target cell heterogeneity and have reached their limit in terms of efficacy. Identification and detailed molecular characterization of tumor-driving cells along with in-depth understanding of the dynamics that govern their phenotype therefore appear to be inescapable requirements for the design of effective anticancer treatment.

Several mechanisms underlie the heterogeneity that characterizes solid malignancies, most prominent among which are clonal selection and hierarchical organization of tumor cells along with the effects of microenvironmental cues (*1*–*3*). Tumor cell plasticity renders the heterogeneity dynamic by allowing cells that drive tumor growth to differentiate and lose their tumorigenic properties in addition to providing the means for nontumorigenic cells to regain tumor-initiating capability (*2*–*4*). It is also key to tumor cell adaptation and resistance to treatment (*2*, *4*, *5*). Comprehensive identification of individual cells and cell subpopulations endowed with the ability to initiate and maintain tumor growth and progression is hampered by their lack of reliable biological markers. Although some cell surface receptors have been useful in isolating cell populations enriched in tumor-initiating cells (*1*, *6*), their ability to identify the full spectrum of cells that drive any given tumor remains limited. Moreover, because cancer cells, at least in some tumor types, may transition between tumorigenic and nontumorigenic phenotypes (*1*, *7*), it stands to reason that any unbiased approach designed to capture them in their tumorigenic state should exploit mechanisms underlying their plasticity in the most appropriate models available.

The recent development of three-dimensional (3D) culture technologies has facilitated assessment of tumor heterogeneity and drug sensitivity in a relevant preclinical setting. Under appropriate culture conditions, tumor-derived primary cells can generate spheroids that retain the native tissue heterogeneity or, as observed in a variety of carcinomas, organoids, which recapitulate both the heterogeneity and architecture of the tissue of origin (*8*–*10*). Primary 3D cultures derived from a variety of cancer types have helped identify major determinants of tumor heterogeneity and uncover therapeutic vulnerabilities that went unrecognized in standard 2D models (*10*, *11*). Moreover, patient-derived tumor 3D culture xenografts (PDXs) currently provide the closest in vivo mimics of the corresponding native tumors (*12*) and are particularly valuable for the study of cancers that lack genetically engineered mouse models. A case in point is Ewing sarcoma (EwS), the second most common bone malignancy in children and young adults (*13*).

EwS is a highly aggressive tumor with a marked tendency to relapse following therapy as well as high metastatic proclivity (*14*). Although multimodal therapy has improved survival of patients with localized disease, metastatic lesions at diagnosis markedly worsen prognosis, reducing the 5-year survival to 25%. EwS is caused by one of several reciprocal chromosomal translocations leading to the formation of a fusion gene that encodes an aberrant transcription factor, the most common, found in 85 to 90% of tumors, being EWS-FLI1 (*15*). The chromosomal translocation is the only detectable genetic event in about 25% of EwS, suggesting that the resulting fusion protein bears dominant, if not sole, responsibility for their

[1]Experimental Pathology Service, Centre Hospitalier Universitaire Vaudois, University of Lausanne, Lausanne, Switzerland. [2]Department of Computational Biology, University of Lausanne, Lausanne, Switzerland. [3]Department of Pathology and Center for Cancer Research, Massachusetts General Hospital and Harvard Medical School, Boston, MA, USA. [4]Broad Institute of MIT and Harvard, Boston, MA, USA. [5]Department of Systems Biology, Harvard Medical School, Boston, MA, USA. [6]Department of Histopathology, Central Institute, Valais Hospital, Sion, Switzerland. [7]Institute of Pathology, Centre Hospitalier Universitaire Vaudois, University of Lausanne, Lausanne, Switzerland. [8]Department of Orthopedics, Faculty of Biology and Medicine, Centre Hospitalier Universitaire Vaudois, Lausanne, Switzerland. [9]Department Woman-Mother-Child, Division of Pediatrics, Centre Hospitalier Universitaire Vaudois, University of Lausanne, Lausanne, Switzerland. [10]Department of Neurosciences Rita Levi Montalcini, University of Turin, Center of Omics Sciences, Ospedale San Raffaele IRCSS, Milan, Italy.
*Corresponding author. Email: ivan.stamenkovic@chuv.ch
†These authors share senior authorship.

pathogenesis. EWS-FLI1 behaves as an aberrant transcriptional regulator that orchestrates major chromatin remodeling and functions as a pioneer factor to establish de novo active enhancers at GGAA microsatellite repeats (*16*). It promotes cell plasticity by deregulating microRNA (miRNA) maturation (*17*) and by directly decreasing miR-145 expression, which plays a prominent role in limiting cell pluripotency in both normal development and cancer (*18*, *19*). Repression of miR-145 contributes to the emergence and maintenance of poorly differentiated cells, which not only initiate primary and metastatic tumor growth but also differentiate into nontumorigenic progeny, thereby fueling tumor heterogeneity (*17*–*19*).

Here, we devised an experimental approach combining the power of miRNA reporter technology with primary 3D models of EwS to identify tumor cell subpopulations endowed with high tumorigenic and prometastatic properties. We leveraged the relationship between down-regulation of miR-145 and increased tumor cell pluripotency in EwS (*18*) to generate an inducible reporter system and isolate live primary miR-145^{high} and miR-145^{low} tumor cells in vivo. Functional analyses showed miR-145^{low} cells to be far more tumorigenic than their miR-145^{high} counterparts and to display a distinct gene expression signature comprising several oncogenes, including the receptor tyrosine kinase (RTK) EPHB2 (Ephrin type-B receptor 2). Current databases show EPHB2 expression to be associated with poor survival among patients with EwS, and our functional assays revealed that EPHB2 plays a critical role in promoting metastasis in EwS. On the basis of the role played by miR-145 in the emergence of undifferentiated and aggressive cells in other tumors, we anticipate our inducible in vivo reporter assay to be widely applicable to diverse cancer types and to facilitate the design of mechanism-based strategies to defeat tumor heterogeneity.

RESULTS

Detection of miR-145 activity in primary EwS cells

Our working strategy is summarized in Fig. 1A. Briefly, primary 3D tumor cell cultures from EwS removed at surgery were engineered to express the miR-145 reporter. Following validation of reporter activity in vitro, the 3D culture–derived tumor cells were transplanted into immunocompromised mice, the resulting tumors were removed, and cells were sorted based on reporter activity. Cells with high and low miR-145 expression could then be assessed for gene expression, clonogenicity, and tumor-initiating capacity following reinjection into mice.

To develop an inducible miR-145 responsive reporter (mirRep145), we engineered a green fluorescent protein (GFP)–encoding sequence containing five consecutive miR-145 recognition motifs in its 3′ untranslated region (3′UTR) and inserted it into the pINDUCER20 plasmid, downstream of the TRE2 promoter (Fig. 1A and fig. S1A) (*20*). An inducible, tetracycline-activated (Tet-On) expression system was chosen to minimize the potential sponge effect of exogenous miRNA binding site overexpression. Administration of doxycycline (Dox) to the cells harboring mirRep145 induced transcription of the GFP reporter sequence, and GFP expression levels were directly dependent on the intrinsic miR-145 activity (by binding to its target sequences, miR-145 suppresses the translation or transcription of the corresponding gene), providing an unbiased means to identify miR-145^{low} (GFP$^+$) and miR-145^{high} (GFP$^-$) cells (Fig. 1A). miR-145 target sequences were substituted by an unrelated DNA sequence to generate a mirReporter-Control vector (mirRepC) (fig. S1B).

mirRep145 was tested in HeLa cells, which express low levels of miR-145. Induction of GFP expression in cells harboring mirRep145 occurred within 48 hours of treatment with Dox, as assessed by confocal microscopy (Fig. 1B and fig. S1C, bottom), and neither mirRep145- nor mirRepC-containing cells expressed GFP in the absence of Dox (Fig. 1B and fig. S1C, top). To validate the specific dependency of our reporter system on miR-145 activity, we tested the effect of unrelated miRNAs on HeLa cells bearing mirRep145 using expression plasmids containing the red fluorescent protein (RFP)–puromycin resistance fusion protein (rPuro), which allows simultaneous assessment of infection efficiency by RFP expression and selecting for puromycin resistance (Fig. 1C, middle). Immunofluorescence microscopy of Dox-treated HeLa mirRep145 cells infected with a mock miRNA sequence (an unrelated sequence matching miR-145 length), let7a-, or miR-145–containing vectors revealed reduced GFP expression only in cells expressing miR-145 (Fig. 1C, right), indicating specific targeting of the reporter GFP construct by miR-145.

We then assessed mirRep145 function in two EwS 3D cultures, EwS1 and EwS2 (*21*–*23*), derived, respectively, from a metastatic lung lesion removed after chemotherapy and an untreated primary tumor (table S1). Both 3D cultures, which appeared as spheroids, retained the hierarchical cellular organization of the primary tumors from which they were derived (*21*, *22*). EwS1 and EwS2 cells infected with a lentivirus containing the mirRep145 were maintained as 3D cultures in medium supplemented with Dox for 48 hours and assessed for GFP expression by flow cytometry and fluorescence microscopy 2 (D2), 5 (D5), and 10 (D10) days following Dox removal (fig. S1, D to G). Fluorescence-activated cell sorting (FACS) revealed that 47 and 38% of the EwS1- and EwS2-mirRep145 cell populations, respectively, were GFP$^+$ after Dox-mediated induction (fig. S1, D and F). GFP expression decreased rapidly following Dox removal and was undetectable after 10 days of Dox-free culture. Neither Dox nor its removal affected 3D spheroid formation in vitro (fig. S1, E and G).

Purification of primary EwS cell subpopulations based on miR-145 expression

We previously showed that EwS cells with low miR-145 expression have clonogenic and tumor-initiating capacity, giving rise to tumors that phenocopy the original tumor, whereas cells with high miR-145 expression from the same tumor were poorly tumorigenic (*17*, *18*). To address the properties of miR-145^{low} EwS cells and identify candidate predictive markers of tumor aggressiveness, we transplanted mirRep145-expressing EwS1 and EwS2 3D culture–derived cells into the subcapsular renal compartment of nonobese diabetic severe combined immunodeficient γ (NSG) mice whose diet was supplemented with appropriate doses of Dox. Upon reaching 1 cm^3, the tumors were removed at autopsy and dissociated, and GFP expression of the cells was assessed by flow cytometry. Both EwS 3D culture–derived tumors displayed induction of GFP expression in vivo, with approximately 21% of EwS1 and 15% of EwS2 cells being GFP$^+$ (Fig. 1D).

Next, we verified that mirRep145 allows separation of tumor cells based on their intrinsic miR-145 expression by quantitative polymerase chain reaction (qPCR) assessment of miR-145 transcripts in sorted GFP$^-$ and GFP$^+$ subpopulations. Consistent with its mechanism of action, expression of miR-145 was almost threefold lower in GFP$^+$ than in GFP$^-$ cells (Fig. 1E). Immunohistochemistry (IHC) using anti-GFP antibody on tumor tissue sections revealed no GFP signal in control tumors but strong expression in a fraction of cells

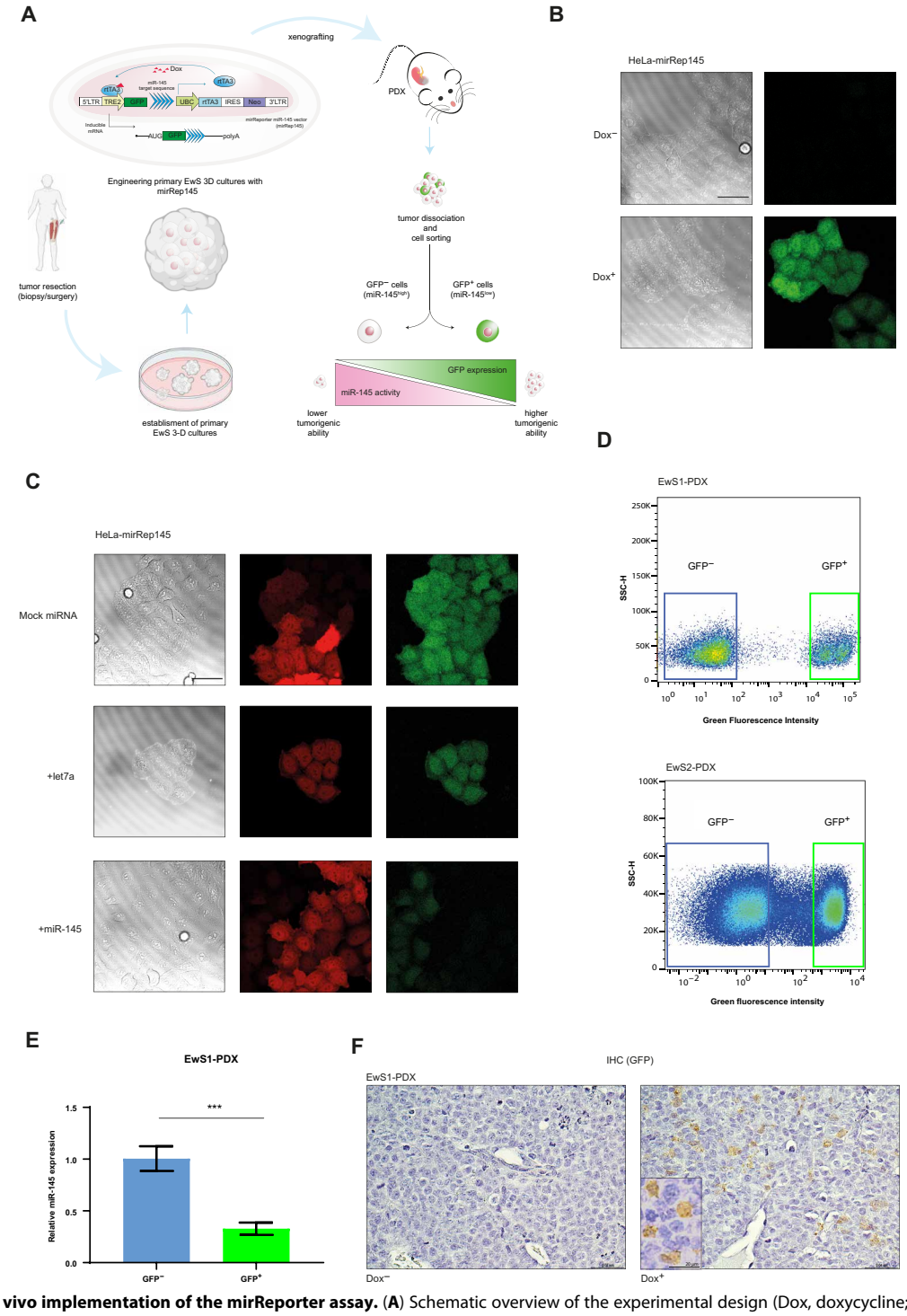

Fig. 1. In vitro and in vivo implementation of the mirReporter assay. (**A**) Schematic overview of the experimental design (Dox, doxycycline; GFP, green fluorescent protein; IRES, internal ribosome entry site; LTR, long terminal repeat; Neo, neomycin; rtTA3, reverse tetracycline-controlled transactivator 3; PDX, patient-derived xenograft; TRE2, Tet response element 2; UBC, ubiquitin C promoter; 5'cap = ●—). (**B**) Representative confocal microscopy images of induced GFP (green) expression in HeLa-mirRep145 cells treated with Dox (1 μg/ml, 48 hours) (bottom) compared to phosphate-buffered saline (PBS)–treated control cells (Dox^-) (top) (40× objective; scale bar, 50 μm). (**C**) Representative confocal microscopy images showing decreased GFP expression (green) in Dox-treated HeLa-mirRep145 cells overexpressing miR-145 compared to HeLa-mirRep145 cells overexpressing mock miRNA and let7a [middle: red fluorescent protein (RFP) expression (red); right: GFP expression (green); 40× objective; scale bar, 50 μm]. (**D**) Fluorescence-activated cell sorting (FACS) based on GFP expression in mirRep145-bearing EwS1-PDX (top) and EwS2-PDX (bottom) cells. (**E**) Quantitative real-time polymerase chain reaction (qRT-PCR) assessment of mature miR-145 expression in GFP^+ and GFP^- subpopulations of EwS1-PDX carrying mirRep145 after in vivo induction, tumor dissociation, and cell sorting. (Mean ± SD values of three technical replicates are shown. Statistical analysis was done by unpaired *t* test; $^{***}P \leq 0.001$.) (**F**) Immunohistochemical assessment of GFP expression in tumor tissues of a EwS1-PDX-mirRep145–injected control mouse (Dox^-) and a Dox-treated mouse (Dox^+) (scale bars, 40 μm; inset scale bar, 20 μm).

in tumors from Dox-fed mice (Fig. 1F and fig. S1H). Dox penetration of the tumor tissue appeared to be adequate, as GFP$^+$ cells were observed throughout the tumor and not merely around blood vessels. miR-145 expression was significantly higher in both EwS1- and EwS2-derived PDXs compared to their corresponding in vitro culture models, confirming the ability of primary 3D culture–derived cells to generate more differentiated progeny in vivo (fig. S1I). On the basis of our earlier observations that miR-145 regulates the pluripotency-associated gene *SOX2* in EwS cells (*18*), we compared *SOX2* expression between bulk EwS1 cells and their GFP$^+$ and GFP$^-$ fractions. Consistent with our previous results, GFP$^+$ cells expressed higher levels of *SOX2* than their GFP$^-$ counterparts (fig. S1J).

Low miR-145 activity as a marker of primary EwS cells in a highly tumorigenic state

We then assessed miR-145^{high} and miR-145^{low} cell tumorigenicity in vivo. MirRep145-infected EwS1 and EwS2 3D culture–derived cells were transplanted beneath the kidney capsule of NSG mice, and tumor growth was monitored by ultrasonography weekly. Mice bearing tumors of about 1 cm^3 were given Dox for 96 hours, after which they were euthanized and tumors were removed. Following dissociation and mouse cell depletion, tumor cells were sorted into GFP$^-$ and GFP$^+$ subpopulations, which were then retransplanted beneath the kidney capsule of NSG mice. Unsorted bulk tumor cells (induced bulk, IB) from Dox-treated animals were transplanted into a third group of mice and tumor growth in all animals was monitored by ultrasonography (Fig. 2A).

Self-renewal of GFP$^-$, GFP$^+$, and bulk cells from Dox-treated (IB) and untreated (control bulk) mice was assessed by clonogenic assays in which sphere formation was scored after 4 weeks of culture. Both EwS1 and EwS2 PDX–derived GFP$^+$ cells displayed higher self-renewal than either batch of bulk or GFP$^-$ cells (Fig. 2B). Consistent with their higher self-renewal, EwS1 and EwS2 GFP$^+$ cells were more tumorigenic than their GFP$^-$ counterparts (Fig. 2, C to G).

To verify mirRep145 stability, aliquots of cells derived from first-round xenografts, including IB, GFP$^+$, and GFP$^-$ cells, were cultured in vitro in the presence of geneticin and Dox. The three cell populations retained resistance to neomycin, whereas only GFP$^+$ and IB tumor–derived populations expressed GFP in response to Dox (fig. S2). MirRep145 therefore remained stably expressed and functional throughout in vivo tumor growth, demonstrating the feasibility of using miR-145 expression as a functional reporter to isolate subpopulations of cells with divergent tumorigenic capacity from a heterogeneous tumor cell population.

A dual-color mirReporter to monitor the evenness of cell infection

To ensure that GFP$^-$ and GFP$^+$ subpopulations reflect endogenous differences in miR-145 expression rather than uneven cell infection, we generated a second mirReporter to monitor infection homogeneity. The RFP-puromycin vector (rPuro, described above) provides both an antibiotic selection marker and the means to track infected cells by monitoring RFP expression. We thus established a miR-145–responsive dual-color reporter assay (Dual mirRep145) in which green fluorescence indicates miR-145 expression and red fluorescence reflects infection homogeneity (Fig. 3A).

Dual mirRep145 expression in HeLa cells (Fig. 3B) revealed that RFP expression was independent of Dox treatment, confirming successful cell infection, and that GFP expression was induced upon Dox administration. Similarly, EwS1 and EwS2 cells harboring Dual mirRep145 expressed RFP and, upon treatment with Dox for 48 hours, initiated GFP while maintaining RFP expression (fig. S3A). Following removal of Dox, EwS1 and EwS2 cells lost GFP expression within 10 days but retained RFP expression, indicating reporter stability.

EwS1 and EwS2 cells carrying Dual mirRep145 were sorted based on their RFP expression (fig. S3B) to select the most homogeneously infected cell population for in vivo tumor initiation assays (Fig. 3C). The selected Dual mirRep145–bearing EwS1 and EwS2 cells were transplanted beneath the kidney capsule of NSG mice, and following tumor formation, mice were administered Dox as before. After tumor dissociation at autopsy, cells were assessed for GFP and RFP expression by flow cytometry (Fig. 3, D and E). EwS1 and EwS2 cells with comparable RFP expression were then sorted based on their GFP levels. The clonogenic and tumorigenic properties of sorted GFP$^-$ and GFP$^+$ cells were assessed in vitro and in vivo, respectively. GFP$^+$ cells displayed higher clonogenicity than their GFP$^-$ counterparts (Fig. 3F and fig. S3C), as well as greater tumor-initiating ability (Fig. 3G and fig S3, D to F). Our observations using Dual mirRep145 were therefore consistent with those obtained using the single-color mirRep145.

Identification of candidate genes that underlie EwS aggressiveness and bear potential prognostic value

To gain insight into the mechanisms underlying the difference in GFP$^+$ (miR-145^{low}) and GFP$^-$ (miR-145^{high}) EwS cell subpopulation behavior, we compared the transcriptome of primary GFP$^+$ and GFP$^-$ cells derived from freshly dissociated EwS1-PDX and EwS2-PDX carrying mirRep145 or Dual mirRep145. All cells sorted according to GFP expression were included into a single statistical mode in which the covariate of interest was GFP expression, denoted as GFP$^+$ and GFP$^-$. The other covariates used for adjustment were the tumor origin (EwS1 or EwS2) and the type of reporter (mirRep145 or Dual mirRep145). DEseq2 was used to fit the model and differentially expressed genes were defined by $|\log FC| > 1$ and a nominal $P < 0.01$. Using these parameters, we found 55 and 29 significantly up- and down-regulated genes, respectively, in GFP$^+$ compared to GFP$^-$ cells (tables S2 and S3). To address a possible link between miR-145 and EWS-FLI-1 expression levels, we compared differentially expressed genes between GFP$^+$ and GFP$^-$ EwS1 cells to those that displayed a change in expression upon *EWSR1-FLI1* depletion by short hairpin RNA (shRNA) in the same model (*23*). However, the observation that the same EWS-FLI-1–dependent gene expression signature was enriched in both GFP$^+$ and GFP$^-$ populations (fig. S4A) does not support the notion of variable EWS-FLI-1 expression between GFP$^+$ and GFP$^-$ cells. In addition, expression of 106 previously described EWS-FLI-1 direct target genes (*23*) was not found to be significantly different between GFP$^+$ and GFP$^-$ cells (fig. S4B), indicating that their distinct behavior was not related to differences in *EWSR1-FLI1* expression or function. Last, no significant enrichment for direct miR-145 targets was identified among differentially expressed genes between GFP$^+$ and GFP$^-$ cells (fig. S4, C and D), suggesting that the signatures distinguishing GFP$^+$ from GFP$^-$ subpopulations are not merely the effect of miR-145 expression but the result of complex transcriptional programs that may define different cell phenotypes.

To determine whether these gene expression signatures may bear any prognostic value, we asked whether the significantly up- and down-regulated genes in the GFP$^+$ subpopulation (miR-145^{low}) are

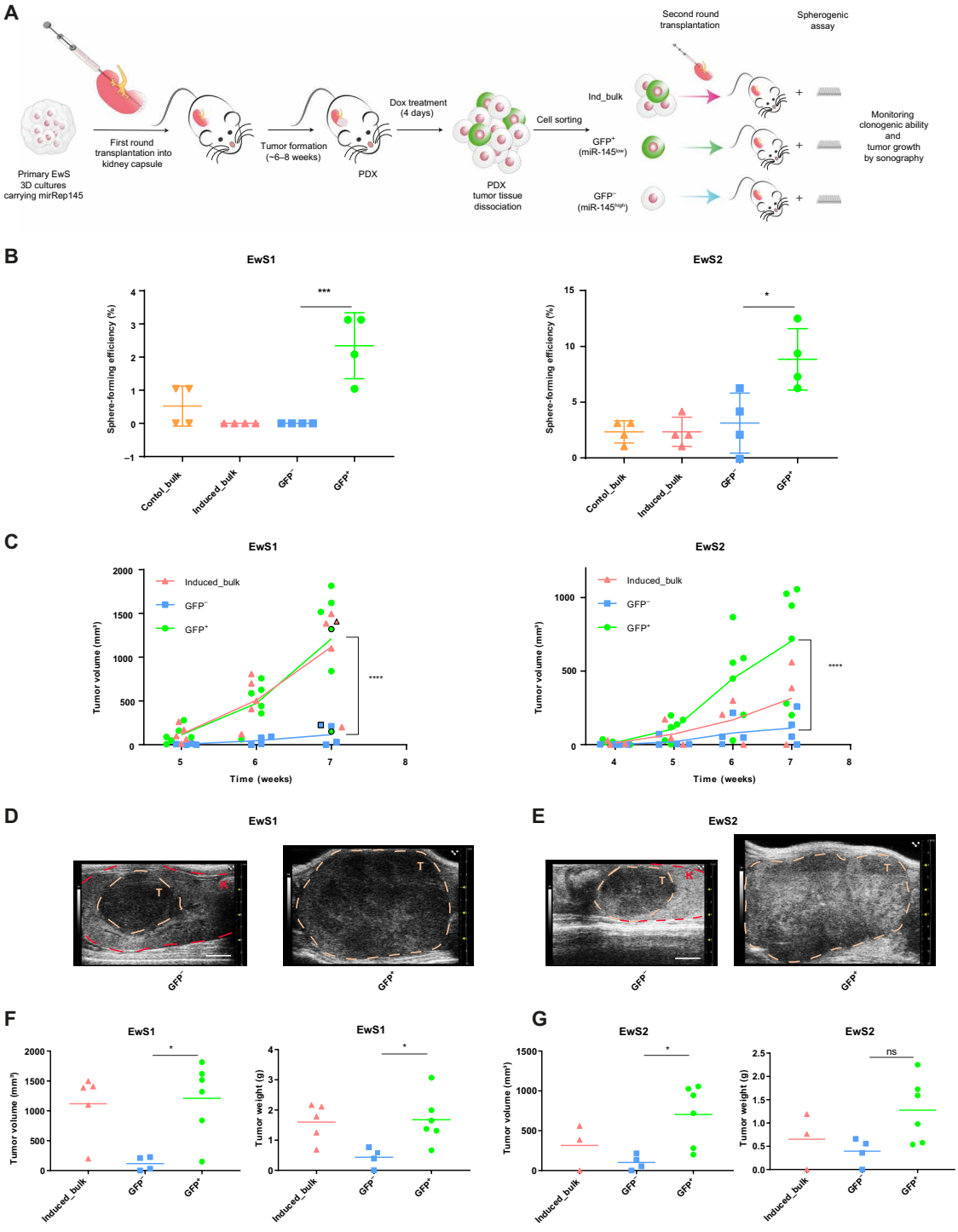

Fig. 2. Primary EwS 3D cultures with low miR-145 expression display high clonogenic capacity in vitro and tumor-initiating capacity in vivo. (**A**) Schematic diagram of the experimental design of in vivo studies. (**B**) GFP$^+$ (miR-145^{low}) subpopulations of EwS1-PDX (left) and EwS2-PDX (right) have higher clonogenic capacity than their GFP$^-$ (miR-145^{high}) counterparts (mean ± SD values of four technical replicates are shown). Control bulk and induced bulk (IB) cells were obtained from PDX-derived tumor tissues of control (drinking water devoid of Dox) and Dox-treated mice (2 mg/ml, 96 hours), respectively. (**C**) In vivo tumorigenicity of GFP$^+$ and GFP$^-$ cells obtained from EwS1-PDX (right) and EwS2-PDX (left). (Average tumor volumes were measured weekly by ultrasonography. EwS1: IB, $n = 5$ mice; GFP$^-$, $n = 4$ mice; GFP$^+$, $n = 6$ mice. EWS2: IB, $n = 3$ mice; GFP$^-$, $n = 4$ mice; GFP$^+$, $n = 6$ mice. Mean ± SD values of technical replicates are shown. Primary tumors whose symbols are outlined in black are shown in Fig. 4G.) (**D** and **E**) Ultrasonograms of GFP$^-$ and GFP$^+$ tumors from EwS1-PDX (D) and EwS2-PDX (E) 6 weeks after injection of cells beneath the kidney capsule (T, tumor tissue; K, kidney tissue; scale bars, 2 mm). (**F** and **G**) The GFP$^+$ subpopulation of EwS1-PDX (F) and EwS2-PDX (G) gave rise to larger tumors than the GFP$^-$ subpopulation (mean ± SD values of technical replicates are shown). [One-way analysis of variance (ANOVA) was used to perform the statistical analysis of (B), (F), and (G), and two-way ANOVA was used for the analysis of (C); ns, not significant; *$P \leq 0.05$; ***$P \leq 0.001$; ****$P \leq 0.0001$.]

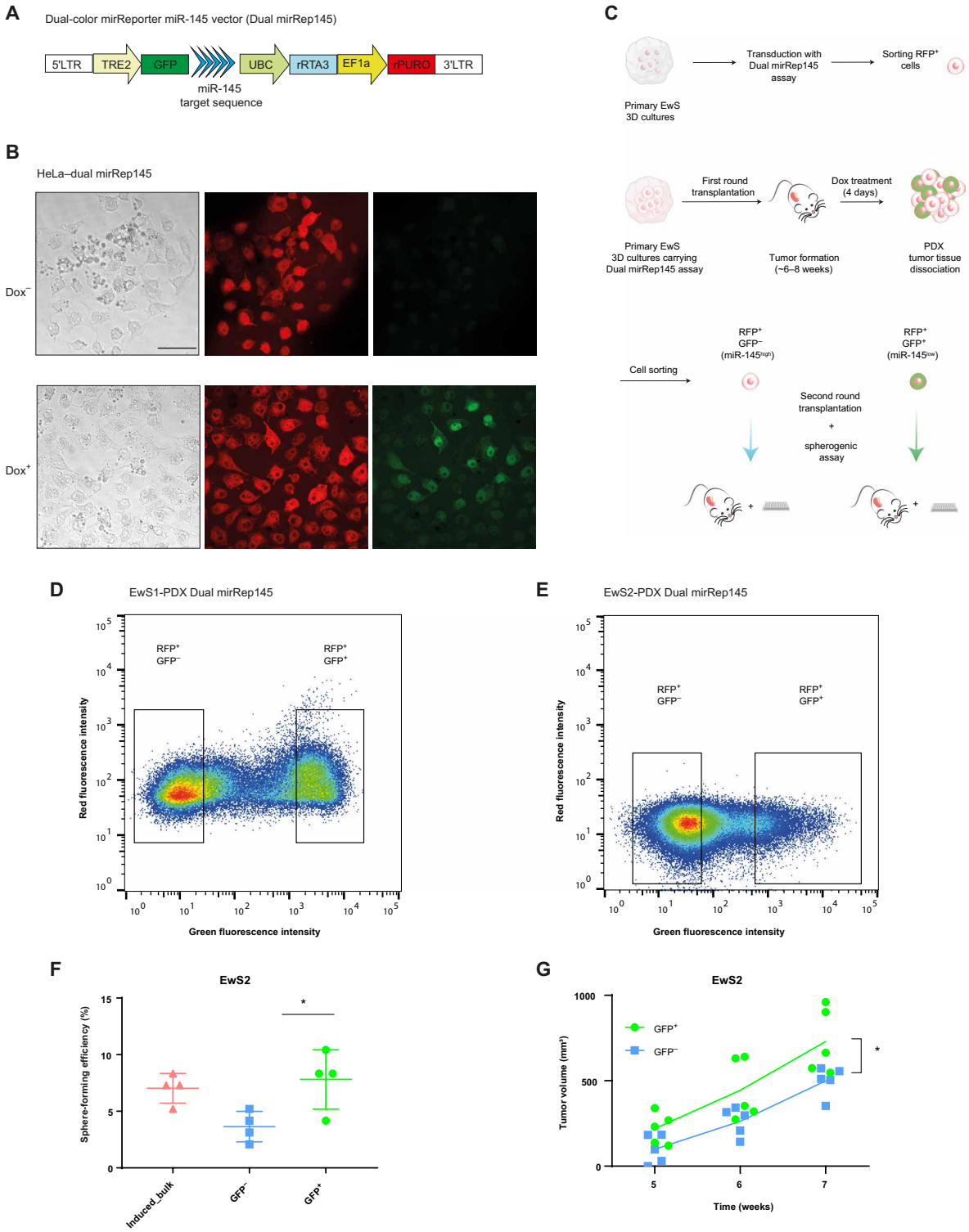

Fig. 3. A dual-color mirReporter allows monitoring cell infection homogeneity. (**A**) Diagram showing the dual-color mirReporter miR-145 construct (Dual mirRep145). (**B**) Representative confocal microscopy images showing Dox-induced (1 μg/ml, 48 hours) GFP expression (green) in HeLa cells carrying the Dual mirRep145 (bottom) compared to PBS-treated control cells (top) [middle: RFP expression (red) indicating the distribution of Dual mirRep145 infection; 40× objective; scale bar, 50 μm]. (**C**) Schematic illustration of the Dual mirRep145 assay design in vitro and in vivo. (**D** and **E**) FACS acquisition of RFP and GFP in Dual mirRep145 carrying EwS1-PDX (D) and EwS2-PDX (E) cells after in vivo induction of reporter expression [mice received Dox (2 mg/ml) for 96 hours before sacrifice and tumor dissociation]. (**F**) GFP$^+$ EwS2-PDX–Dual mirRep cells are more clonogenic than their GFP$^-$ counterparts. [Mean ± SD values of four technical replicates are shown. IB: dissociated tumor cells from mice treated with Dox (2 mg/ml) for 96 hours.] (**G**) Tumors derived from EwS2-PDX GFP$^+$ cells grow faster than tumors originating from the corresponding GFP$^-$ cells ($n = 5$ mice per group). [One-way ANOVA test was used to perform the statistical analysis of (F) and two-way ANOVA was used for the analysis of (G); *$P \leq 0.05$.]

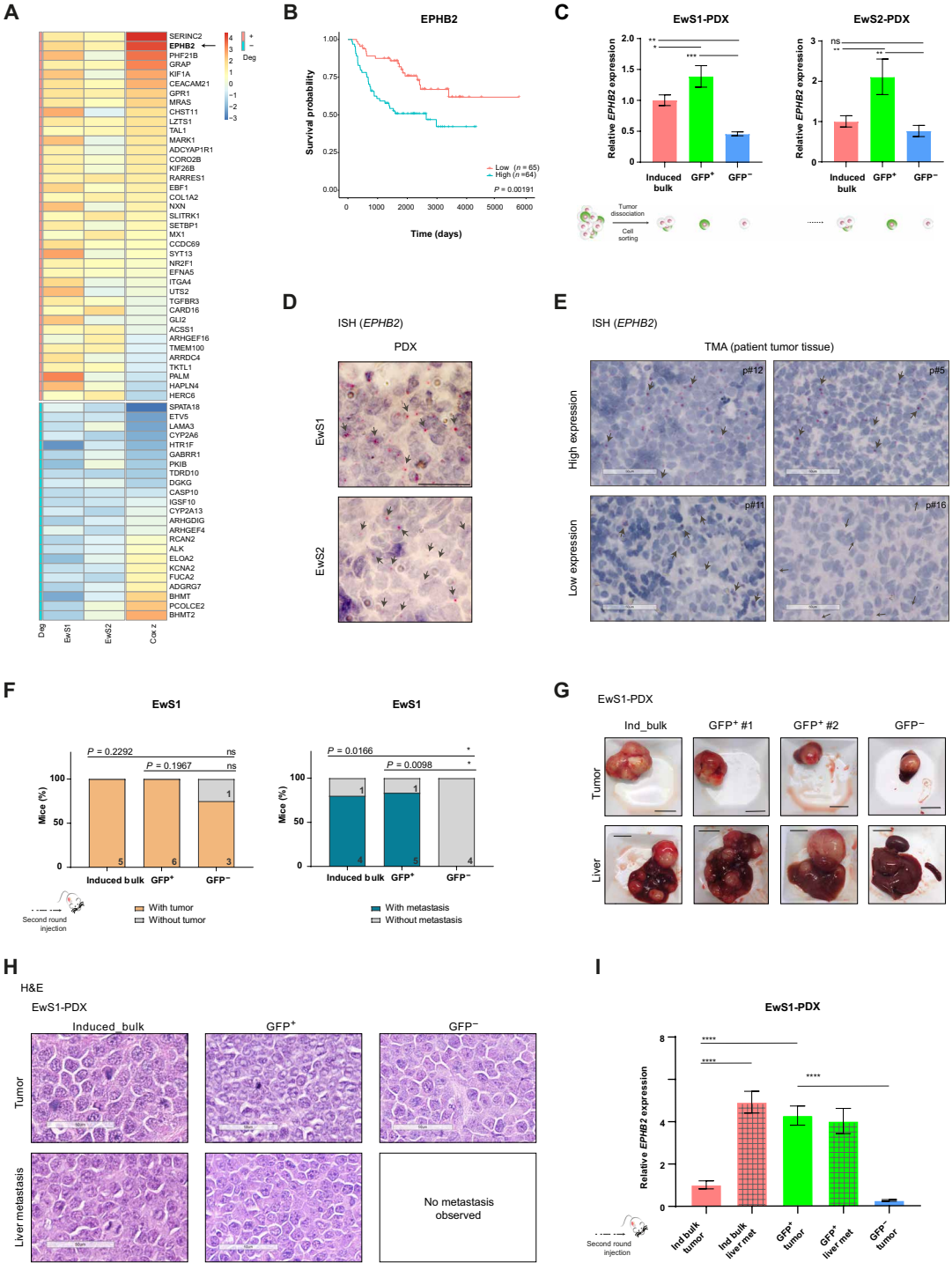

Fig. 4. Identification of EPHB2 as a candidate gene that underlies EwS aggressiveness with a potential prognostic value. (**A**) Heatmap of differentially expressed genes in the GFP$^+$ subpopulation of EwS-PDXs (compared to GFP$^-$ counterparts). The Cox *z* values (and sign) indicate the strength of the positive correlation between the expression level of a gene and patient survival. (**B**) Kaplan-Meier curves showing overall survival of patients with high and low *EPHB2* expression. (**C**) Relative *EPHB2* expression in IB, GFP$^+$, and GFP$^-$ subpopulations of EWS1 and EWS2 PDX (mean ± SD values of three technical replicates are shown). (**D**) RNA in situ hybridization (ISH) assessment of *EPHB2* expression in EwS-PDX tissues (scale bar, 25 μm) and (**E**) in primary EwS tumors (scale bars, 50 μm; arrows indicate ISH signals). (**F**) Distribution of local tumor– and metastasis-bearing mice following injection of the indicated cell subpopulations (IB, $n = 5$; GFP$^+$, $n = 6$; GFP$^-$, $n = 4$) with (**G**) representative pictures of primary tumors and matched livers (scale bars, 1 cm). (Corresponding primary tumor volume symbols are outlined in Fig. 2C. Photo credit: Tugba Keskin, CHUV.) (**H**) Representative H&E (hematoxylin and eosin)–stained sections of local tumors and matched liver metastases (scale bars, 50 μm). (**I**) qRT-PCR assessment of *EPHB2* transcripts in primary tumors and their matched liver metastases (mean ± SD values of three technical replicates are shown). [One-way ANOVA test was used to perform the statistical analysis of (C) and (I), log-rank (Mantel-Cox) was used for (B), and chi-square (Fisher's exact test) was used for (F). ns, not significant; $*P \leq 0.05$; $**P \leq 0.01$; $***P \leq 0.001$; $****P \leq 0.0001$.]

predictive of survival for patients with EwS. We combined five different primary EwS microarray datasets into a single dataset containing survival details of 129 patients. To assess putative predictive values of significantly down- and up-regulated genes in GFP$^+$ cells on overall EwS patient survival, we performed univariate Cox analysis of the correlation between the gene expression level and survival duration. Such analysis produces a *z* value, which indicates the strength and sign of the correlation for significantly up- and down-regulated genes in the highly tumorigenic miR-145^{low} EwS cells. We found that up-regulated genes had mostly positive *z* values (Fig. 4A), indicating correlation between their expression and adverse prognosis, whereas the opposite was true of down-regulated genes. To validate these observations, Kaplan-Meier survival analysis was performed in the same cohort by comparing two clusters of patients with individual gene expression below (n = 65) and above (n = 64) the median value. A significant negative correlation was observed between expression of the up-regulated gene *EPHB2* (P = 0.00191) and survival (Fig. 4B).

EPHB2 encodes a transmembrane RTK that binds ephrin ligands and mediates intercellular communication through bidirectional signaling (*24*). Several arguments support its functional implication in promoting EwS cell aggressiveness. First, its expression in GFP$^+$ cells was about four times higher than in GFP$^-$ cells (table S2). Second, EwS patients bearing tumors with high *EPHB2* expression levels have worse overall survival rates (Cox z = 4.102, Cox $P = 4.09 \times 10^{-5}$, Kaplan Meier P = 0.00191) than patients with tumors expressing low levels of the gene (Fig. 4, A and B). Third, EPHB2 plays a well-established role in both maintaining cell pluripotency and promoting carcinogenesis (*25*) and is implicated in tumor metastasis (*26*).

We therefore assessed *EPHB2* expression in EwS1 and EwS2 PDX-derived cell fractions and observed significantly higher expression of *EPHB2* in GFP$^+$ than in GFP$^-$ and IB cells in both 3D culture models (Fig. 4C). RNA in situ hybridization (ISH) analysis of EwS1 and EwS2 xenografts showed a marked difference in their *EPHB2* expression pattern, with relatively diffuse expression in EwS1 xenografts versus paucicellular expression in EwS2 (Fig. 4D). These observations reflect *EPHB2* expression heterogeneity in EwS, in terms of both level and cell percentage, as illustrated by *EPHB2* RNA ISH analysis of a cohort of 16 primary EwS patient samples (Fig. 4E and fig. S4E).

On the basis of the prognostic value of EPHB2 in patients with EwS and the notion that the major clinical determinant of EwS patient survival is their metastatic burden, we reasoned that EPHB2 may be involved in EwS dissemination. Consistent with our hypothesis, we observed a notable difference in metastatic spread among sorted cell populations. Following the second round of injection, tumors developed in all mice injected with GFP$^+$ and IB cells from EwS1 PDX and in 75% of the mice injected with GFP$^-$ cells (Fig. 4F). However, whereas large liver metastases formed in 80 and 83.33% of mice injected with IB and GFP$^+$ cells, respectively, none of the mice injected with GFP$^-$ cells developed visible metastases (Fig. 4F). This discrepancy did not appear to be due to differences in tumor growth at the site of injection because one EwS1 GFP$^+$ tumor whose size was comparable to those of GFP$^-$ tumors was associated with large liver metastases (Figs. 4, G and H, and 2C). Expression of *EPHB2* was elevated in the liver metastases derived from both IB and GFP$^+$ tumors, as well as in GFP$^+$ tumors at the site of injection. By contrast, it was low in IB tumors at the injection site and undetectable in GFP$^-$ tumors (Fig. 4I).

EPHB2, a candidate marker of EwS cells with self-renewing and metastatic properties

To determine its functional role in EwS self-renewal and tumor initiation, we partially depleted EwS1 cells of EPHB2 using lentiviral vectors bearing two different EPHB2-specific shRNAs (Fig. 5, A and B). Compared to controls, cells depleted of EPHB2 exhibited a dramatic decrease in spheroid formation in vitro (Fig. 5C) and a correspondingly impaired ability to initiate tumor growth in vivo (Fig. 5, D to F). ISH and qPCR assessment of tumors that emerged from EPHB2-depleted cell xenografts revealed their expression of *EPHB2* at levels comparable to those of control cells, suggesting that they originated from cells that had evaded *EPHB2* depletion (Fig. 5, G and H). To circumvent the technical limitations inherent to shRNAs, we generated CRISPR-mediated EPHB2 knockout (KO) EwS1 cells using three different single guide RNAs (sgRNAs) targeting *EPHB2*. The resulting EPHB2-depleted EwS1 cells displayed markedly reduced clonogenicity (Fig. 6, A to C). To address the possible involvement of EPHB2 in pro-metastatic properties of GFP$^+$ EwS1 cells, we addressed the invasiveness of EPHB2 KO cells in vitro, as assessed by Matrigel transwell assays. We observed that invasiveness was strongly impaired in the absence of EPHB2 (Fig. 6D).

To determine whether our functional observations reflect a general property of EwS, we interrogated the Cancer Cell Line Encyclopedia for EPHB2 expression levels in EwS cell lines and selected two, A673 and RD-ES, for further investigation based on their robust expression of the receptor. Both cell lines were grown as spheroids in ultralow attachment plates to mimic the primary models. After validation of its expression by FACS analysis (fig. S5, A and B), we depleted EPHB2 from both lines by shRNA and measured the ensuing changes in their clonogenicity and invasiveness in vitro. We observed a significant decrease in the clonogenicity and invasiveness of both cell lines upon EPHB2 depletion, supporting our findings in the primary EwS1 model (Fig. 6, E to H, and fig. S5, C to F).

In contrast to EwS1, EwS2 bulk and GFP$^+$ cells formed only microscopic metastases (fig. S6, A to C). A possible explanation for the difference in behavior between EwS1 and EwS2 cells may lie in their origin: Unlike EwS1 cells, which were derived from a metastatic tumor to the lung following chemotherapy, EwS2 cells originated from a primary, untreated tumor and only few expressed EPHB2 (Fig. 4D and table S1). We reasoned that if EPHB2 is involved in fueling the metastatic properties of EwS cells, enhancement of its expression in weakly metastatic primary tumor cells may promote their dissemination, similar to EwS1. Exogenous overexpression of EPHB2 in EwS2 cells (Fig. 7, A and B, and fig. S6D) did not alter their self-renewal or tumor-initiating ability (Fig. 7, C to F, and fig. S6E). In contrast, whereas EwS2 control cells did not form macroscopic metastases, EwS2 cells expressing exogenous EPHB2 formed multiple large metastases in several organs, particularly the liver, lung, contralateral kidney, and peritoneum (Fig. 7, G to J, and fig. S6, F and G). Careful histological examination revealed that control EwS2 cells were able to form a small number of micrometastases in the lung and kidney, often centered by blood vessels (Fig. 7J, left). However, in the absence of EPHB2 overexpression, no macro-metastases arose for the duration of the experiments. Together, our results indicate that EPHB2 promotes the metastatic properties of primary EwS cells, raising the possibility that pharmacological targeting of its signaling pathway may provide a candidate strategy to blunt EwS dissemination.

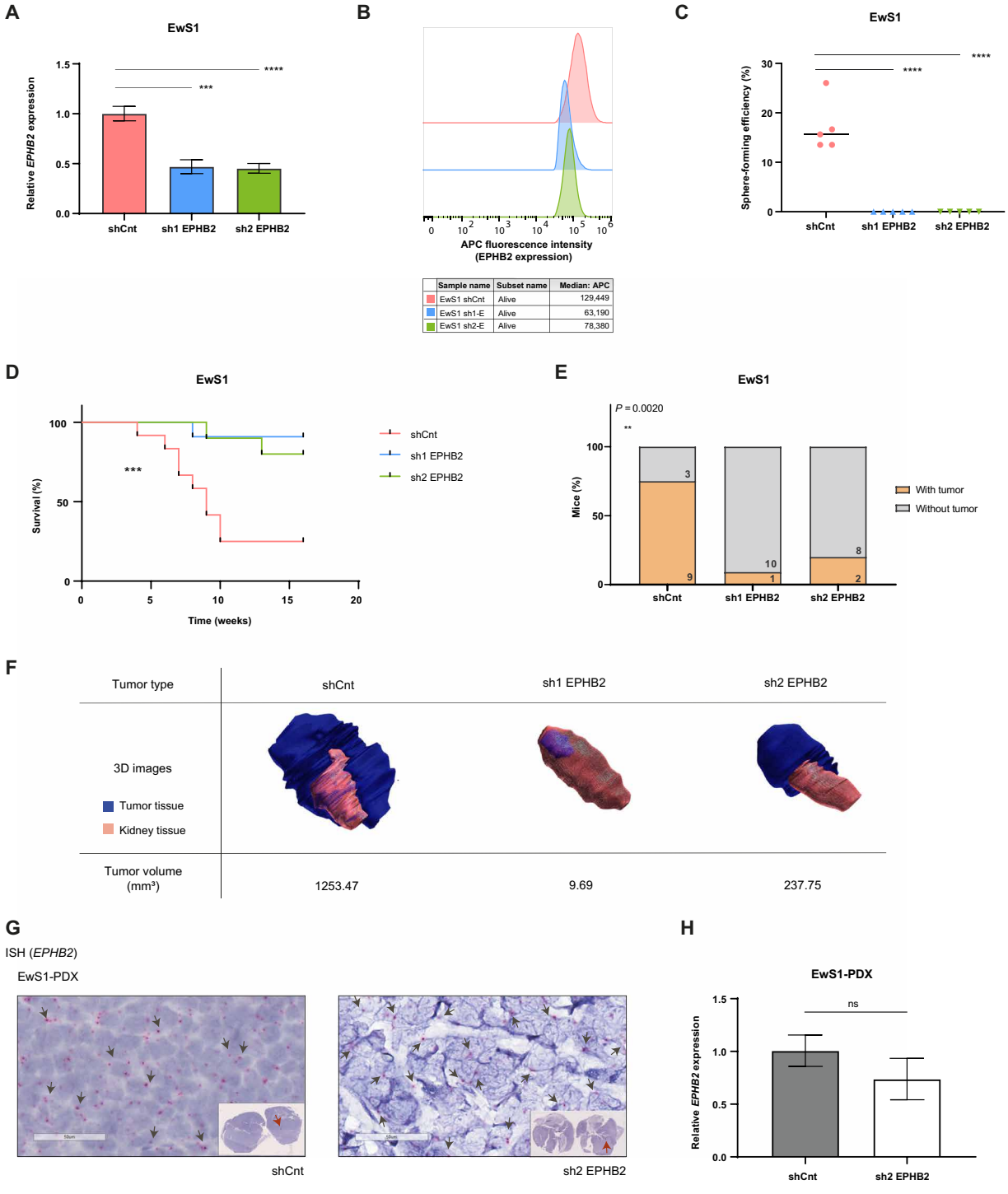

Fig. 5. EPHB2 depletion impairs tumor growth in vivo. (**A**) Relative *EPHB2* expression of EwS1 3D culture infected with EPHB2-targeting shRNAs (sh1 EPHB2 and sh2 EPHB2) compared to those in EwS1 control cells transduced with GFP-targeting shRNA (shCnt) as measured by qRT-PCR (mean ± SD, $n = 3$). (**B**) EPHB2 expression, as assessed by flow cytometry, in EwS1 3D cultures following shRNA-mediated EPHB2 depletion compared to EwS1 control cells (shCnt). (**C**) Clonogenic assay of EwS1 3D cultures depleted of EPHB2 (mean ± SD, $n = 5$). (**D**) Survival of mice injected with EwS1 3D cultures depleted of EPHB2 compared to mice injected with EwS1 control 3D culture (shCnt) (shCnt, $n = 12$; sh1 EPHB2, $n = 11$; sh2 EPHB2, $n = 10$). (**E**) EPHB2 depletion reduces the tumorigenic capacity of EwS1 3D culture (corresponding mouse numbers in each group are indicated in the graph bars). (**F**) Representative 3D ultrasonography reconstruction images of tumors at week 7 with corresponding tumor volumes (in cubic millimeters) below. (**G**) RNA ISH and (**H**) qRT-PCR assessment of *EPHB2* transcript expression in tumors derived from EwS1-shCnt and EwS1-sh2 EPHB2 xenografts indicate that the tumors initially depleted of EPHB2 regain its expression (scale bars, 50 μm; arrows indicate ISH signals. qRT-PCR: mean ± SD, $n = 3$). [One-way ANOVA test was used to perform the statistical analysis of (A), (C), and (H); log-rank (Mantel-Cox) was used for (D); and chi-square (Fisher's exact test) was used for (E). ns, not significant; $^{**}P \leq 0.01$; $^{***}P \leq 0.001$; $^{****}P \leq 0.0001$.]

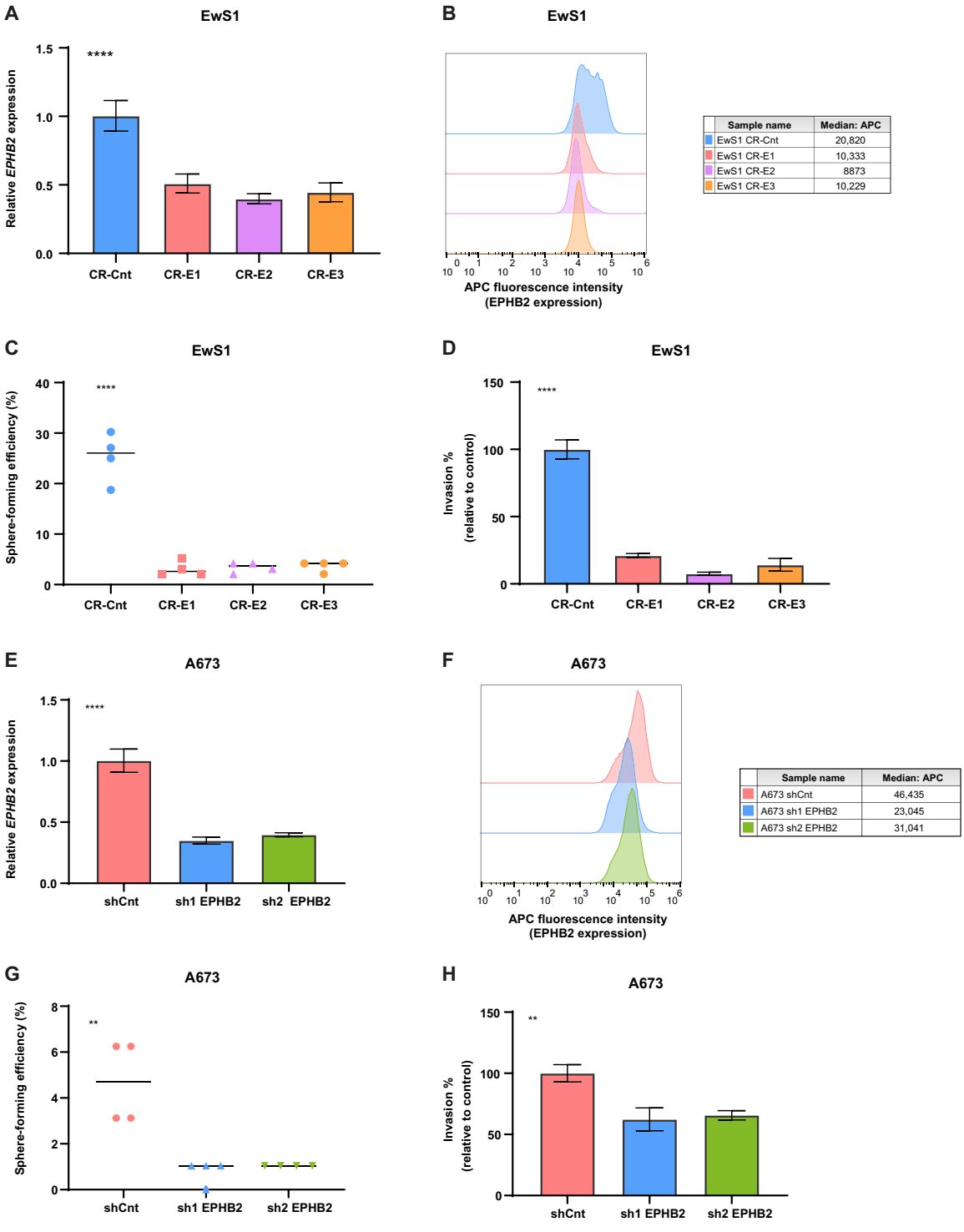

Fig. 6. EPHB2 depletion reduces clonogenicity and invasiveness of EwS cells. (**A**) Relative *EPHB2* expression of EwS1 3D culture infected with EPHB2-targeting sgRNAs (CR-E1, CR-E2, and CR-E3) compared to EwS1 control cells (CR-Cnt) as measured by qRT-PCR (mean ± SD values of three technical replicates are shown). (**B**) EPHB2 expression, as assessed by flow cytometry, in EwS1 3D cultures following sgRNA-mediated EPHB2 depletion in (A). (**C**) Clonogenic and (**D**) transwell-invasion assays for EwS1 tumor 3D cultures depleted of EPHB2 (CR-E1, CR-E2, and CR-E3) compared to control cells (CR-Cnt) (mean ± SD values of four and three technical replicates are shown for clonogenic and invasion assays, respectively). (**E**) qRT-PCR and (**F**) FACS analysis of EPHB2 expression in the EwS A673 cell line transduced with *EPHB2* targeting shRNAs (sh1 EPHB2 and sh2 EPHB2) compared to control cells (shCnt). (**G**) Clonogenic and (**H**) transwell-invasion assays for A673 cells depleted of EPHB2 (sh1 EPHB2 and sh2 EPHB2) compared to control cells (shCnt) (mean ± SD values of four and three technical replicates are shown for clonogenic and invasion assays, respectively). [One-way ANOVA test was used for statistical analysis of (A), (C), (D), (E), (G), and (H); $^{**}P \leq 0.01$; $^{****}P \leq 0.0001$.]

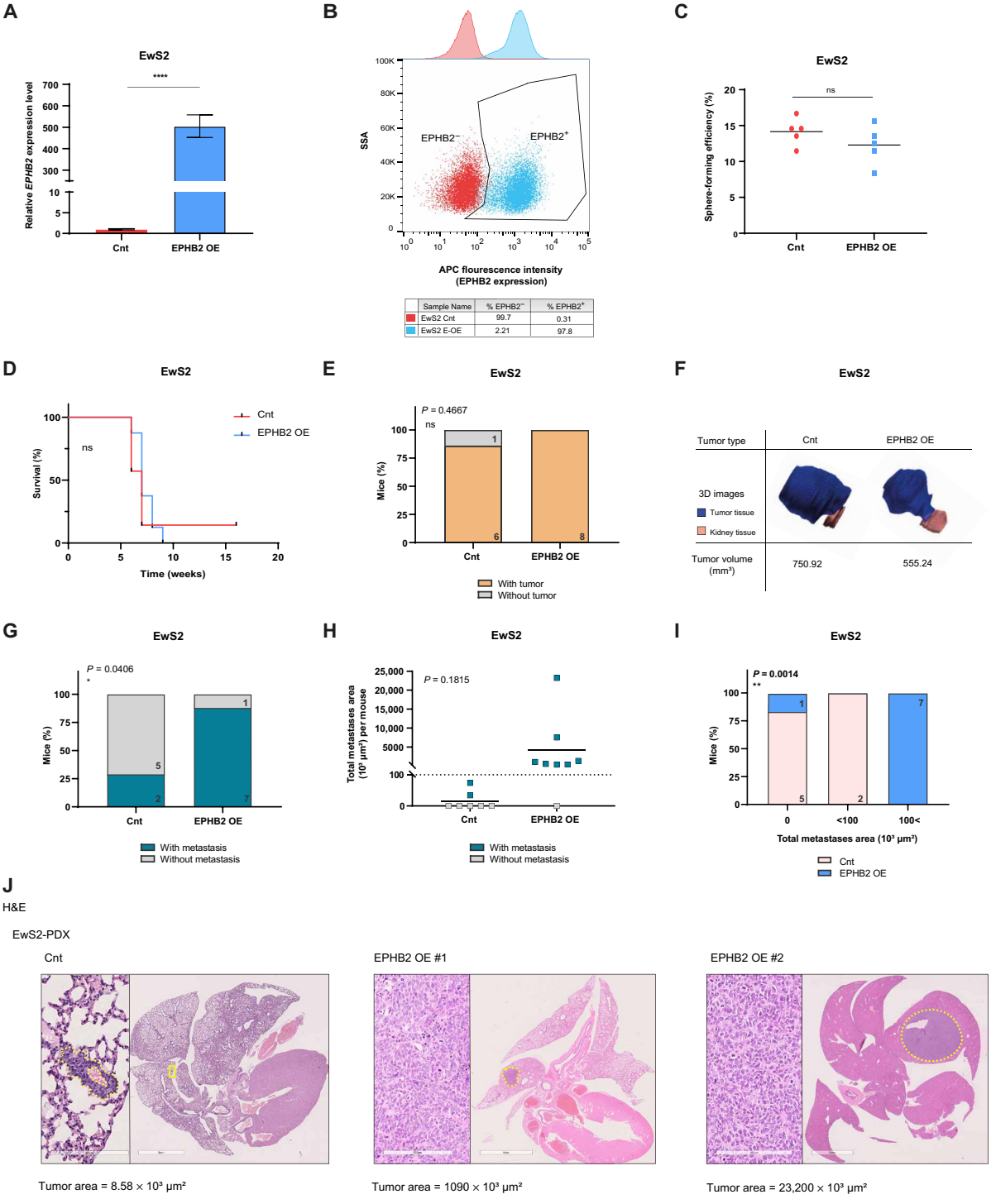

Fig. 7. EPHB2 overexpression increases EwS2 3D culture invasiveness. (**A**) qRT-PCR and (**B**) FACS assessment of EPHB2 expression in EwS2 cells overexpressing EPHB2 (EPHB2 OE) compared to control cells (Cnt). (**C**) Clonogenic assay of EwS2 EPHB2 OE and Cnt cells (mean ± SD values of five technical replicates are shown). (**D**) Survival of mice injected with EwS2 EPHB2 OE or EwS2 control 3D cultures (Cnt) (Cnt, $n = 7$; EPHB2 OE, $n = 8$). (**E**) Percentage of mice developing tumors following injection with the indicated EwS2 3D cultures (Cnt, $n = 7$; EPHB2 OE, $n = 8$). (**F**) Representative 3D sonography reconstruction images of EwS2 EPHB2 OE and EwS2 Cnt tumors. (**G**) Overexpression of EPHB2 significantly increased metastasis of EwS2 cells (Cnt, $n = 7$; EPHB2 OE, $n = 8$). (**H**) The total area of EwS2 metastases per mouse increased as a result of EPHB2 overexpression (mean ± SD. Cnt, $n = 7$; EPHB2 OE, $n = 8$). (**I**) Mice injected with EwS2 EPHB2 OE had a significantly higher metastatic burden than mice injected with control EwS2 cells (Cnt, $n = 7$; EPHB2 OE, $n = 8$). (**J**) Representative H&E sections of lung and liver metastases in mice injected with EwS2 EPHB2 OE compared to animals injected with control EwS2 cells (scale bars, Cnt: 200 µm, 3 mm; EPHB2 OE#1: 200 µm, 4 mm; EPHB2 OE#2: 200 µm, 5 mm). [One-way ANOVA test was used to perform the statistical analysis of (A), (C), and (H); log-rank (Mantel-Cox) was used for (D); and chi-square (Fisher's exact test) was used for (E), (G), and (I). ns, not significant; $*P \leq 0.05$, $**P \leq 0.01$, $****P \leq 0.0001$.]

DISCUSSION

Elucidation of the biological properties of cells responsible for tumor initiation, maintenance, and progression is key for the development of effective cancer therapies. However, in most cancer types, identification of these cells has been limited by reliance on predefined, largely nonspecific cell surface markers (*27*). Although helpful in uncovering subpopulations of cells enriched in those endowed with pluripotency and tumor-initiating ability, currently used markers fall short of accurately identifying the cells that actually display such properties. To overcome these limitations and isolate cells that represent the driving force of tumorigenesis, we developed a functional reporter assay, using as a model, EwS, in which a small fraction of cells display pluripotency and hold at least part of the responsibility for tumor initiation and phenotypic heterogeneity (*21*, *22*).

In EwS (*16*–*18*), and probably most pediatric cancers (*28*–*32*), cellular heterogeneity is generated primarily by epigenetic forces, which include histone modifications, DNA methylation, and miRNA expression. Because they are key players in the fine-tuning of cancer cell phenotypes by regulating pluripotency and differentiation, miRNAs are well suited to generate powerful candidate reporter systems. The level of their expression may not only be a reliable reflection of cell phenotypes that are pertinent to aggressive or indolent tumor behavior but also associate with gene expression networks that contribute to that behavior and help identify the relevant genes. On the basis of the dynamics of its expression according to the degree of tumor cell pluripotency or differentiation, we selected miR-145 to generate a reporter designed to reflect a spectrum of cancer cell phenotypes and identify those of interest. Using the reporter to target cells with low miR-145 expression in EwS, we identified highly tumorigenic subpopulations with metastatic properties.

Of the small number of deregulated genes shared by miR-145^{low} cell subpopulations from two independent primary tumors, *EPHB2* appeared immediately relevant, as its expression is associated with poor prognosis in EwS according to existing databases. The expression pattern was divergent between our two 3D culture models, being relatively diffuse in EwS1, which was derived from a metastatic tumor, but limited to only a small number of cells in EwS2, obtained from a primary tumor. Reminiscent of their tumors of origin, EwS1 formed macroscopic metastases following subcapsular renal injection of NSG mice, whereas EwS2 formed micrometastases composed of only a small number of cells, preferentially located around blood vessels in the lung and contralateral kidney in a fraction of mice. Overexpression of EPHB2 in EwS2 cells drove them to form macrometastases in several organs, providing a clear indication that EPHB2 expression participates in driving EwS metastatic proclivity.

EPHB2 expression is associated with the development and progression of diverse tumor types (*33*–*35*) and may facilitate metastasis by enhancing angiogenesis (*36*), modifying tumor cell adhesion and migration (*35*, *37*) and promoting invasion (*38*). Our present observations raise the possibility that the level of EPHB2 expression among metastatic tumor cells may determine their emergence from dormancy and/or adaption to the newly colonized microenvironment.

Our study suggests that diverse and complementary approaches may be required to dissect tumor heterogeneity at a functional level. Single-cell studies of EwS suggested that fluctuations in *EWSR1-FLI1* expression levels might underlie diverse biological properties among tumor cell subpopulations, including proliferation and metastatic proclivity (*39*, *40*). These observations, coupled to the notion that *EWSR1-FLI1* is a miR-145 target (*18*), would be consistent with variable EWS-FLI-1 expression levels as an explanation for the differences in tumorigenic behavior of GFP$^+$ and GFP$^-$ populations within our primary models. However, our comparative gene expression analysis of EWS-FLI-1 targets and GFP$^+$/GFP$^-$ signatures did not support this hypothesis. The absence of a clear miR-145 target gene signature in the differential transcriptional profile between GFP$^+$ and GFP$^-$ cells suggests that complex transcriptional programs, to which miR-145 expression is associated, govern the biological properties of these subpopulations and underlie their phenotypes. In support of this notion, expression of the miR-145 target *SOX2*, an important player in cell pluripotency, was elevated in GFP$^+$ cells. EPHB2, on the other hand, is not a miR-145 target but rather an effector component of the expression profile of EwS cells with low miR-145 levels, which in turn reflects a cellular phenotype associated with high metastatic proclivity.

A potential limitation of the present study is the use of only two primary tumor-derived EwS 3D cultures. Generation of primary 3D cultures from sarcomas, and EwS in particular, has been challenging, which explains the small number of currently available 3D EwS cultures. However, we confirmed our observations using two established cell lines grown as spheroids. Another limitation is the current lack of pharmacological inhibitors of the EPHB2 receptor, which restricted our assessment of the effect of its inhibition to observations based on its shRNA-mediated depletion. Given that EPHB2 is an RTK, however, development of pharmacological inhibitors should be possible.

These limitations notwithstanding, we have shown that combining a miRNA-based functional reporter system with primary tumor 3D culture technology provides a powerful and reliable method to isolate and characterize tumor cells that display aggressive behavior, including the formation of metastasis. MirRep145 allowed us to identify EPHB2 as a mediator of EwS metastasis that can be used both as a predictor of tumor behavior and as a potential therapeutic target to eliminate the most aggressive cells. The instructive role of miR-145 in cell fate transitions during cancer initiation and progression supports our strategy as an unbiased approach to explore and target tumor heterogeneity in diverse cancer types without the requirement of a predefined marker.

MATERIALS AND METHODS

Plasmid construction

Tet-On inducible mirReporter expression vectors were constructed using the Gateway LR Clonase II Enzyme Mix (Thermo Fisher Scientific). pINDUCER20 (Addgene, #44012) and pENTR/D-TOPO (Thermo Fisher Scientific) were the destination and entry vectors, respectively.

The coding sequence of enhanced GFP (EGFP) was amplified by PCR using pcDNA3-EGFP (Addgene, #13031) as template and EGFP-F and EGFP-R primers. The amplified EGFP cDNA sequence, which included a 3′UTR containing three miR-145 recognition sites, was cloned into the Bst BI and Mlu I restriction sites of the pLIV lentiviral vector (*23*). An EGFP cDNA containing five miR-145 recognition sites was subsequently generated by inserting two more miR-145 target sequences (oligo DNA A and oligo DNA B; table S4) into the Mlu I and Bam HI cloning site in the pLIV-EGFP vector containing the three miR-145 target sequence repeats. The resulting sequence was PCR-amplified using the primer pairs TOPO-F and TOPO-R (table S4), and the PCR product was cloned into the

pENTR/D-TOPO plasmid for subsequent pInducer20 gateway cloning. The target sequence of hs-mir-145-5p was obtained from the online tool mirbase.org (MIMAT0000437). MirReporter-Control was created by replacing the hs-mir-145-5p target sequence with the 3′UTR sequence of glyceraldehyde-3-phosphate dehydrogenase [National Center for Biotechnology Information (NCBI) Reference Sequence: NM_001256799.3; sequence position: 1186-1313].

The dual-color mirReporter–miR-145 vector was obtained by replacing the neomycin cassette and the internal ribosome entry site sequence with the coding sequence of rPuro and the EF (elongation factor)-1α promoter, respectively. The double-stranded synthetic DNA fragment (IDT) containing the rPuro coding sequence taken from the pLV-mir-control plasmid (catalog no. mir-p000, Biosettia) was inserted into the Nde I and Ssp I cloning site of mirReporter-145. Next, a DNA synthetic fragment (IDT) bearing the EF-1α promoter sequence was cloned into the Nde I and Spf I site. The synthetic DNA fragment sequences are available upon request.

Establishment of primary tumor 3D cultures and cell culture

EwS tumor samples were obtained from consenting patients with the approval of the ethics committee of the Canton de Vaud (Authorization No. 260/15). Primary tumor 3D cultures were established following immediate mechanical and enzymatic dissociation of the tumor samples. Red blood cells (RBCs) were removed using RBC lysis buffer (Miltenyi Biotec), and tumor cells were resuspended in Iscove's modified Dulbecco's medium (Gibco) containing KO serum (20%; Gibco), recombinant human EGF (10 ng/ml; Invitrogen), recombinant human FGF (10 ng/ml; Invitrogen), and penicillin-streptomycin (1%; Gibco) in ultralow attachment flasks (Corning). Once established, tumor cell 3D cultures were disrupted into single-cell suspensions manually with a P1000 pipette, and early passages were cryopreserved. EwS1 and EwS2 cultures were passaged every 7 and 4 days, respectively. In this study, EwS1 and EwS2 3D cultures ranged between passages 4 to 15 and 15 to 30, respectively.

HeLa cells [American Type Culture Collection (ATCC)] and A673 cells (ATCC) were cultured in Dulbecco's modified Eagle's medium (DMEM) (Gibco) whereas RD-ES cells (ATCC) were grown in RPMI (Gibco) supplemented with fetal bovine serum (FBS) (10%, PAN-Biotech) and penicillin-streptomycin (1%; Gibco). Human embryonic kidney (HEK) 293T cells (ATCC) were cultured in DMEM (Gibco) supplemented with FBS (10%; PAN-Biotech), MEM nonessential amino acid (Gibco), and penicillin-streptomycin (1%; Gibco). Cell cultures were maintained at 37°C in humidified, 5% CO_2 chambers. Spheroids of A673 and RD-ES cells were grown in ultralow attachment plates (Corning) and used in clonogenic and Matrigel-invasion assays.

Lentiviral infection and in vitro induction

For lentiviral production, HEK 293T cells (ATCC) were transfected using FuGENE 6 Transfection Reagent (Promega). pMD2G (Addgene, #12259) and pCMVΔR8.74 (Addgene, #12263) vectors were used as envelope and packaging plasmids, respectively. Lentiviral harvest was performed using Lenti-X Concentrator (TAKARA). Single-cell suspensions from primary EwS 3D cultures were infected with lentivirus expressing mirReporter-Control, mirReporter–miR-145, or dual-color mirReporter–mir-145. HeLa cells were infected for overexpression of mock-miRNA-rPuro (catalog no. mir-p000, Biosettia), mir-let7a-rPuro (catalog no. mir-p001, Biosettia), and mir-145-rPuro (catalog no. mir-p116, Biosettia). Transduced cells were selected by geneticin (1 mg/ml; Gibco) and puromycin (1 μg/ml; Invivogen) for 7 and 3 days, respectively, before further analysis.

EPHB2 depletion was achieved using pLKO.1 lentiviral shRNAs purchased from the RNAi Consortium (sh1 ref.: TRCN0000006423; sh2 ref.: TRCN0000006425), and sgRNAs targeting *EPHB2* (CR-E1, CR-E2, and CR-E3) were designed using the online CRISPR tool box CHOPCHOP (*41*) and cloned into the lentiCRISPRv2 vector. sgRNA target sequences were as follows: CR-E1: ACCAAGTTTATCCGGCGCCGTGG; CR-E2: AGAAGACACGCACGGCGATGAGG; and CR-E3: GTCCGGCTGGGACCACGACA-GGG. In EPHB2 knockdown studies, control cells were infected with shRNA or sgRNA sequences targeting the GFP transcript (GCAAGCTGACCCTGAAGTTCAT). For EPHB2 overexpression, a plasmid carrying EPHB2 cDNA sequence under the EF-1α promoter (catalog no. EX-E2379-Lv156) and its control plasmid expressing EGFP cDNA (catalog no. EX-EGFP-Lv156) were purchased from GeneCopoeia.

Light and fluorescent microscopy

Primary EwS 3D cultures were treated with Dox (100 ng/ml) (Sigma-Aldrich) for 48 hours and cultured for 10 days. Representative images were acquired using a Nikon Eclipse TS100 inverted epifluorescence microscope with ultraviolet lamp and filters set to 488 and 561 nm to detect GFP and RFP, respectively. HeLa cells seeded on coverslips (10 mm, VWR) were treated with Dox (1 μg/ml) for 48 hours. After fixation (4% formaldehyde, 10 min at room temperature) and mounting, slides were imaged by Zeiss Confocal Fluorescent Microscope LSM710 at 40×/1.30 numerical aperture oil immersion.

RNA extraction and real-time PCR

Total RNA extraction was performed using a miRCURYTM RNA Isaltion Kit (Exiqon). Five hundred nanograms of RNA template was used for cDNA synthesis (miRCURYTM LNA Universal RT miRNA PCR, Universal cDNA Synthesis Kit II, Exiqon).

Real-time PCR amplification was done using Power SYBR Green PCR Master Mix (Applied Biosystems) in a QuantStudio 5 System instrument (Thermo Fisher Scientific). PCR conditions included an initial holding period at 50°C for 2 min and 95°C for 10 min followed by 95°C for 15 s and 60°C for 1 min for 40 cycles. RNA LNA (Exiqon) primer sets were used for hsa-mir-145-5p and endogenous control Snord49a amplification. The EPHB2 primer pair was selected according to PrimerBank (http://pga.mgh.harvard.edu/primerbank) (PrimerBank ID: 111118977c1; table S4). Ribosomal protein lateral stalk subunit P0 transcript expression was used as the endogenous control (table S4). Relative quantitation of gene expression data was conducted according to the $2^{-\Delta\Delta Ct}$ method.

Flow cytometry

After 48 hours of Dox treatment, the culture medium of the induced cells was replaced with fresh medium and cells were kept in culture for 10 days [after 48-hour induction, halting Dox treatment at D0 (Day 0) and verifying GFP expression at D2, D5, and D10]. To assess EPHB2 levels, cells were labeled with APC (AlloPhycoCyanin) Mouse Anti-Human EPHB2 (BD Pharmingen). APC Mouse Immunoglobulin G1 (IgG1), K isotype antibody was used for control cell labeling. Calcein violet 450 acetoxymethyl (AM) (Thermo Fisher Scientific) labeling dye was used to detect live cells. The fluorescence intensity of GFP, violet AM, and APC was acquired by a Gallios (B43618, Beckman Coulter) cytometer with FL1, FL9, and FL6.

In vivo experiments, cell sorting, and tumor monitoring

All animal experiments were approved by the Animal Experimentation Ethics Committee of the Veterinary Service of the Canton of Vaud (Etat de Vaud, Service Vétérinaire), under authorization number VD2488.1. Ten thousand cells derived from dissociated EwS1 and EwS2 3D cultures in 20 µl of medium were injected beneath the renal capsule of 4- to 8-week-old, female NSG-KO mice. Tumor growth was monitored by ultrasound imaging using a 40-MHz probe and the Vevo 2100 ultrasound machine (VisualSonics). Tumor volumes were calculated by $V = 4/3\ p(\mathrm{Dd} \times \mathrm{Ds} \times \mathrm{Dt})/8$ (Dd: tumor height; Ds: tumor length in long axis; Dt: tumor length in short axis), and animals were euthanized when the tumor volume reached 1 cm^3. Mice received Dox (2 mg/ml) (Sigma-Aldrich) and 5% sucrose (Sigma-Aldrich) in drinking water starting 96 hours before sacrifice. After dissection, tumor fragments removed from each tumor bulk were fixed in 4% paraformaldehyde and processed for hematoxylin and eosin (H&E) staining and RNA ISH. The remaining tumor tissue was dissociated using a tumor dissociation kit (Miltenyi Biotec) by gentleMACS dissociator (Miltenyi Biotec). RBCs were removed by RBC lysis buffer (Miltenyi Biotec), and human tumor cells were enriched by depletion of mouse cells using a mouse cell depletion kit (Miltenyi Biotec). Before sorting GFP^+ and GFP^- cell populations by a Moflo Astrios EQ cell sorter (Beckman Coulter), dissociated tumor cells were treated with Calcein AM (Thermo Fisher Scientific) live-cell labeling dye and 4′,6-diamidino-2-phenylindole (DAPI) (Biotium) to remove dead cells. The sorted GFP^+ and GFP^- cell populations were injected beneath the renal capsule of NSG mice, and tumor growth was monitored by ultrasonography weekly.

Clonogenic and invasion assay

Spheroids generated from freshly dissociated patient-derived xenografts (PDX) and EwS cell lines A673 and RD-ES were sorted as single cells into 96-well plates (ultralow attachment; Corning) at one cell per well using a Moflo Astrios EQ cell sorter (Beckman Coulter). Calcein AM (Thermo Fisher Scientific) and DAPI (BIOTIUM) were used for live-cell detection. Sphere formation was monitored and scored 4 weeks after sorting.

Invasion assays were done according to the manufacturer's instructions (Corning Biocoat Matrigel Invasion Chamber). Briefly, 50,000 single cells were cultured in serum-free medium in the upper chamber of the transwell, whereas the lower chamber was filled with medium supplemented in KO serum. After 48 hours of culture, the cells in the upper chamber were removed and those in the lower layer of insert membranes were stained, and the membranes were mounted onto glass slides. Cells were counted using a Fiji-ImageJ program.

IHC and RNA ISH

Formalin-fixed, paraffin-embedded PDX tumors and mouse organs were sliced into 5-µm sections and subjected to standard H&E staining or IHC to detect GFP expression. RNAscope technology [Advanced Cell Diagnostics (ACD)] was used for RNA ISH according to the manufacturer's instructions as described previously (*42*). Briefly, tissue sections on slides were baked for 1 hour at 60°C, deparaffinized, and dehydrated. The tissues were pretreated with hydrogen peroxide for 10 min at room temperature and with target retrieval reagent for 15 min at 98°C. Protease Plus was then applied for 30 min at 40°C. EPHB2 probe (ACD) was hybridized for 2 hours at 40°C, followed by signal amplification. Tissue was counterstained with Gill's hematoxylin followed by mounting with VectaMount mounting media (Vector Laboratories). Images were taken with a Hamamatsu NanoZoomer S60 Digital slide scanner, at ×40 magnification.

Analysis of RNA sequencing data and relevance to survival

RNA sequencing (RNA-seq) library preparation was performed according to the Illumina TruSeq protocol by IGE3 genomic platform of University of Geneva. RNA-Seq was performed using HiSeq 4000 Illumina.

Reads were aligned to the human genome (NCBI-hg38) using hisat2 with default parameters. Gene-level counts for each sample were obtained with featureCounts against the hg38 RefSeq transcriptome. DeSeq2 was used to determine genes differentially expressed between GFP^+ and GFP^- cells, correcting for tumor 3D culture of origin and type of reporter. Differentially expressed genes were defined by $|\mathrm{logFC}| > 1$ and nominal P value < 0.01.

Five microarray datasets of primary EwS [GEO accession numbers: GSE12102 (*43*), GSE17618 (*44*), GSE34620 (*45*), and GSE63155 and GSE63156 (*46*)] were combined into a single dataset using the brainarray CDFs (Chip Definition Files) and ComBat from the sva package to remove batch effects. Normalization was performed with the SCAN.UPC package that provides a convenient interface for normalization with alternative CDFs and batch correction with ComBat.

For the differentially expressed genes for which expression data from the integrated dataset were available, we performed two types of survival analysis: Cox univariate analysis using expression as a continuous variable and Kaplan-Meier analysis after dividing the samples in two groups. [The median expression of *EPHB2* was used as the cutoff to divide the patients (n = 129) into high (n = 64) and low (n = 65) expressors.]

The heatmap in Fig. 4A shows, for all differentially expressed genes for which Cox univariate analysis was performed, the logarithmic fold change in the two primary tumor 3D cultures [difference in log2(RPKM + 1) between GFP^+ and GFP^- cells, averaged over all experiments on each tumor 3D culture] and the Cox z value. Up-regulated (down-regulated) genes are ordered by decreasing (increasing) Cox z.

Overlaps of differentially expressed genes with gene lists obtained from the literature or databases were statistically assessed using Fisher's exact test, with all genes analyzed by DeSeq2 as the universe. The list of direct EWS-FLI1 targets was obtained from (*42*), while predicted targets of miRNAs were obtained from TargetScan through the targetscan.Hs.eg.db Bioconductor package. For miRNA targets, no overlap was significant after correcting for multiple testing (Benjamini-Hochberg false discovery rate).

Statistical analysis and software used

GraphPad Prism (version 7) program was used to generate graphs and to perform one-way analysis of variance (ANOVA), Student's t test, two-way ANOVA, and log-rank (Mantel-Cox) test analyses. Analyses of flow cytometry acquisition data were done by FlowJo (version 10) program. qRT-PCR data were collected by QuantStudio design and analyses software (version 1.4.2). IHC and RNA ISH images were analyzed by AperioImageScope (v12.1.0.5029) and NDP. View2 Viewing software (U12388-01). biorender.com and Adobe illustrator (2020) programs were used to create the figures. Bioinformatic analysis was performed with R and its packages "survival," "SCAN.upc" (*47*), "sva," "Rsubread" (*48*), and "DESeq2" (*49*).

SUPPLEMENTARY MATERIALS

Supplementary material for this article is available at http://advances.sciencemag.org/cgi/content/full/7/27/eabf9394/DC1

View/request a protocol for this paper from *Bio-protocol*.

REFERENCES AND NOTES

1. J. A. Magee, E. Piskounova, S. J. Morrison, Cancer stem cells: Impact, heterogeneity, and uncertainty. *Cancer Cell* **21**, 283–296 (2012).
2. E. Batlle, H. Clevers, Cancer stem cells revisited. *Nat. Med.* **23**, 1124–1134 (2017).
3. K. Hinohara, K. Polyak, Intratumoral heterogeneity: More than just mutations. *Trends Cell Biol.* **29**, 569–579 (2019).
4. S. Yuan, R. J. Norgard, B. Z. Stanger, Cellular plasticity in cancer. *Cancer Discov.* **9**, 837–851 (2019).
5. A. Marusyk, M. Janiszewska, K. Polyak, Intratumor heterogeneity: The Rosetta Stone of therapy resistance. *Cancer Cell* **37**, 471–484 (2020).
6. D. Nassar, C. Blanpain, Cancer stem cells: Basic concepts and therapeutic implications. *Annu. Rev. Pathol.* **11**, 47–76 (2016).
7. J. E. Visvader, G. J. Lindeman, Cancer stem cells: Current status and evolving complexities. *Cell Stem Cell* **10**, 717–728 (2012).
8. O. Kopper, C. J. de Witte, K. Lõhmussaar, J. E. Valle-Inclan, N. Hami, L. Kester, A. V. Balgobind, J. Korving, N. Proost, H. Begthel, L. M. van Wijk, S. A. Revilla, R. Theeuwsen, M. van de Ven, M. J. van Roosmalen, B. Ponsioen, V. W. H. Ho, B. G. Neel, T. Bosse, K. N. Gaarenstroom, H. Vrieling, M. P. G. Vreeswijk, P. J. van Diest, P. O. Witteveen, T. Jonges, J. L. Bos, A. van Oudenaarden, R. P. Zweemer, H. J. G. Snippert, W. P. Kloosterman, H. Clevers, An organoid platform for ovarian cancer captures intra- and interpatient heterogeneity. *Nat. Med.* **25**, 838–849 (2019).
9. N. Sachs, H. Clevers, Organoid cultures for the analysis of cancer phenotypes. *Curr. Opin. Genet. Dev.* **24**, 68–73 (2014).
10. M. Bleijs, M. van de Wetering, H. Clevers, J. Drost, Xenograft and organoid model systems in cancer research. *EMBO J.* **38**, e101654 (2019).
11. J. Drost, H. Clevers, Organoids in cancer research. *Nat. Rev. Cancer* **18**, 407–418 (2018).
12. D. Tuveson, H. Clevers, Cancer modeling meets human organoid technology. *Science* **364**, 952–955 (2019).
13. T. Z. Minas, D. Surdez, T. Javaheri, M. Tanaka, M. Howarth, H.-J. Kang, J. Han, Z.-Y. Han, B. Sax, B. E. Kream, S.-H. Hong, H. Çelik, F. Tirode, J. Tuckermann, J. A. Toretsky, L. Kenner, H. Kovar, S. Lee, E. A. Sweet-Cordero, T. Nakamura, R. Moriggl, O. Delattre, A. Üren, Combined experience of six independent laboratories attempting to create an Ewing sarcoma mouse model. *Oncotarget* **8**, 34141–34163 (2017).
14. N. Riggi, M. L. Suvà, I. Stamenkovic, Ewing's sarcoma. *N. Engl. J. Med.* **384**, 154–164 (2021).
15. O. Delattre, J. Zucman, B. Plougastel, C. Desmaze, T. Melot, M. Peter, H. Kovar, I. Joubert, P. de Jong, G. Rouleau, A. Aurias, G. Thomas, Gene fusion with an ETS DNA-binding domain caused by chromosome translocation in human tumours. *Nature* **359**, 162–165 (1992).
16. N. Riggi, B. Knoechel, S. M. Gillespie, E. Rheinbay, G. Boulay, M. L. Suvà, N. E. Rossetti, W. E. Boonseng, O. Oksuz, E. B. Cook, A. Formey, A. Patel, M. Gymrek, V. Thapar, V. Deshpande, D. T. Ting, F. J. Hornicek, G. P. Nielsen, I. Stamenkovic, M. J. Aryee, B. E. Bernstein, M. N. Rivera, EWS-FLI1 utilizes divergent chromatin remodeling mechanisms to directly activate or repress enhancer elements in Ewing sarcoma. *Cancer Cell* **26**, 668–681 (2014).
17. C. De Vito, N. Riggi, S. Cornaz, M.-L. Suvà, K. Baumer, P. Provero, I. Stamenkovic, A TARBP2-dependent miRNA expression profile underlies cancer stem cell properties and provides candidate therapeutic reagents in Ewing sarcoma. *Cancer Cell* **21**, 807–821 (2012).
18. N. Riggi, M.-L. Suvà, C. De Vito, P. Provero, J.-C. Stehle, K. Baumer, L. Cironi, M. Janiszewska, T. Petricevic, D. Suvà, S. Tercier, J.-M. Joseph, L. Guillou, I. Stamenkovic, EWS-FLI-1 modulates miRNA145 and SOX2 expression to initiate mesenchymal stem cell reprogramming toward Ewing sarcoma cancer stem cells. *Genes Dev.* **24**, 916–932 (2010).
19. N. Xu, T. Papagiannakopoulos, G. Pan, J. A. Thomson, K. S. Kosik, MicroRNA-145 regulates OCT4, SOX2, and KLF4 and represses pluripotency in human embryonic stem cells. *Cell* **137**, 647–658 (2009).
20. K. L. Meerbrey, G. Hu, J. D. Kessler, K. Roarty, M. Z. Li, J. E. Fang, J. I. Herschkowitz, A. E. Burrows, A. Ciccia, T. Sun, E. M. Schmitt, R. J. Bernardi, X. Fu, C. S. Bland, T. A. Cooper, R. Schiff, J. M. Rosen, T. F. Westbrook, S. J. Elledge, The pINDUCER lentiviral toolkit for inducible RNA interference in vitro and in vivo. *Proc. Natl. Acad. Sci. U.S.A.* **108**, 3665–3670 (2011).
21. M. L. Suva, N. Riggi, J.-C. Stehle, K. Baumer, S. Tercier, J.-M. Joseph, D. Suvà, V. Clément, P. Provero, L. Cironi, M.-C. Osterheld, L. Guillou, I. Stamenkovic, Identification of cancer stem cells in Ewing's sarcoma. *Cancer Res.* **69**, 1776–1781 (2009).
22. S. Cornaz-Buros, N. Riggi, C. DeVito, A. Sarre, I. Letovanec, P. Provero, I. Stamenkovic, Targeting cancer stem–like cells as an approach to defeating cellular heterogeneity in Ewing sarcoma. *Cancer Res.* **74**, 6610–6622 (2014).
23. T. Keskin, A. Bakaric, P. Waszyk, G. Boulay, M. Torsello, S. Cornaz-Buros, N. Chevalier, T. Geiser, P. Martin, A. Volorio, S. Iyer, A. Kulkarni, I. Letovanec, S. Cherix, G. M. Cote, E. Choy, A. Digklia, M. Montemurro, I. Chebib, P. G. Nielsen, A. M. Carcaboso, J. Mora, R. Renella, M. L. Suvà, C. Fusco, P. Provero, M. N. Rivera, N. Riggi, I. Stamenkovic, LIN28B underlies the pathogenesis of a subclass of Ewing sarcoma LIN28B control of EWS-FLI1 stability. *Cell Rep.* **30**, 4567–4583.e5 (2020).
24. E. B. Pasquale, Eph receptors and ephrins in cancer: Bidirectional signalling and beyond. *Nat. Rev. Cancer* **10**, 165–180 (2010).
25. M. Genander, J. Frisen, Ephrins and Eph receptors in stem cells and cancer. *Curr. Opin. Cell Biol.* **22**, 611–616 (2010).
26. J. Potratz, A. Tillmanns, P. Berning, E. Korsching, C. Schaefer, B. Lechtape, C. Schleithoff, R. Unland, K.-L. Schäfer, C. Müller-Tidow, H. Jürgens, U. Dirksen, Receptor tyrosine kinase gene expression profiles of Ewing sarcomas reveal ROR1 as a potential therapeutic target in metastatic disease. *Mol. Oncol.* **10**, 677–692 (2016).
27. T. Klonisch, E. Wiechec, S. Hombach-Klonisch, S. R. Ande, S. Wesselborg, K. Schulze-Osthoff, M. Los, Cancer stem cell markers in common cancers—Therapeutic implications. *Trends Mol. Med.* **14**, 450–460 (2008).
28. C. Kadoch, G. R. Crabtree, Reversible disruption of mSWI/SNF (BAF) complexes by the SS18-SSX oncogenic fusion in synovial sarcoma. *Cell* **153**, 71–85 (2013).
29. M. F. Roussel, J. L. Stripay, Epigenetic drivers in pediatric medulloblastoma. *Cerebellum* **17**, 28–36 (2018).
30. J. Gojo, B. Englinger, L. Jiang, J. M. Hübner, M. L. Shaw, O. A. Hack, S. Madlener, D. Kirchhofer, I. Liu, J. Pyrdol, V. Hovestadt, E. Mazzola, N. D. Mathewson, M. Trissal, D. Lötsch, C. Dorfer, C. Haberler, A. Halfmann, L. Mayr, A. Peyrl, R. Geyeregger, B. Schwalm, M. Mauermann, K. W. Pajtler, T. Milde, M. E. Shore, J. E. Geduldig, K. Pelton, T. Czech, O. Ashenberg, K. W. Wucherpfennig, O. Rozenblatt-Rosen, S. Alexandrescu, K. L. Ligon, S. M. Pfister, A. Regev, I. Slavc, W. Berger, M. L. Suvà, M. Kool, M. G. Filbin, Single-cell RNA-seq reveals cellular hierarchies and impaired developmental trajectories in pediatric ependymoma. *Cancer Cell* **38**, 44–59.e9 (2020).
31. C. Savary, A. Kim, A. Lespagnol, V. Gandemer, I. Pellier, C. Andrieu, G. Pagès, M.-D. Galibert, Y. Blum, M. de Tayrac, Depicting the genetic architecture of pediatric cancers through an integrative gene network approach. *Sci. Rep.* **10**, 1224 (2020).
32. M. G. Filbin, I. Tirosh, V. Hovestadt, M. K. L. Shaw, L. E. Escalante, N. D. Mathewson, C. Neftel, N. Frank, K. Pelton, C. M. Hebert, C. Haberler, K. Yizhak, J. Gojo, K. Egervari, C. Mount, P. van Galen, D. M. Bonal, Q. D. Nguyen, A. Beck, C. Sinai, T. Czech, C. Dorfer, L. Goumnerova, C. Lavarino, A. M. Carcaboso, J. Mora, R. Mylvaganam, C. C. Luo, A. Peyrl, M. Popović, A. Azizi, T. T. Batchelor, M. P. Frosch, M. Martinez-Lage, M. W. Kieran, P. Bandopadhayay, R. Beroukhim, G. Fritsch, G. Getz, O. Rozenblatt-Rosen, K. W. Wucherpfennig, D. N. Louis, M. Monje, I. Slavc, K. L. Ligon, T. R. Golub, A. Regev, B. E. Bernstein, M. L. Suvà, Developmental and oncogenic programs in H3K27M gliomas dissected by single-cell RNA-seq. *Science* **360**, 331–335 (2018).
33. R. A. Johnson, K. D. Wright, H. Poppleton, K. M. Mohankumar, D. Finkelstein, S. B. Pounds, V. Rand, S. E. S. Leary, E. White, C. Eden, T. Hogg, P. Northcott, S. Mack, G. Neale, Y. D. Wang, B. Coyle, J. Atkinson, M. DeWire, T. A. Kranenburg, Y. Gillespie, J. C. Allen, T. Merchant, F. A. Boop, R. A. Sanford, A. Gajjar, D. W. Ellison, M. D. Taylor, R. G. Grundy, R. J. Gilbertson, Cross-species genomics matches driver mutations and cell compartments to model ependymoma. *Nature* **466**, 632–636 (2010).
34. C. Goparaju, J. S. Donington, T. Hsu, R. Harrington, N. Hirsch, H. I. Pass, Overexpression of EPH receptor B2 in malignant mesothelioma correlates with oncogenic behavior. *J. Thorac. Oncol.* **8**, 1203–1211 (2013).
35. A. H. Sikkema, W. F. A. den Dunnen, E. Hulleman, D. G. van Vuurden, G. Garcia-Manero, H. Yang, F. J. G. Scherpen, K. R. Kampen, E. W. Hoving, W. A. Kamps, S. H. Diks, M. P. Peppelenbosch, E. S. J. M. de Bont, EphB2 activity plays a pivotal role in pediatric medulloblastoma cell adhesion and invasion. *Neuro Oncol.* **14**, 1125–1135 (2012).
36. S. Sato, S. Vasaikar, A. Eskaros, Y. Kim, J. S. Lewis, B. Zhang, A. Zijlstra, A. M. Weaver, EPHB2 carried on small extracellular vesicles induces tumor angiogenesis via activation of ephrin reverse signaling. *JCI Insight* **4**, e132447 (2019).
37. S. D. Wang, P. Rath, B. Lal, J.-P. Richard, Y. Li, C. R. Goodwin, J. Laterra, S. Xia, EphB2 receptor controls proliferation/migration dichotomy of glioblastoma by interacting with focal adhesion kinase. *Oncogene* **31**, 5132–5143 (2012).
38. S. Chukkapalli, M. Amessou, A. K. Dilly, H. Dekhil, J. Zhao, Q. Liu, A. Bejna, R. D. Thomas, S. Bandyopadhyay, T. A. Bismar, D. Neill, L. Azoulay, G. Batist, M. Kandouz, Role of the EphB2 receptor in autophagy, apoptosis and invasion in human breast cancer cells. *Exp. Cell Res.* **320**, 233–246 (2014).
39. M.-M. Aynaud, O. Mirabeau, N. Gruel, S. Grossetête, V. Boeva, S. Durand, D. Surdez, O. Saulnier, S. Zaïdi, S. Gribkova, A. Fouché, U. Kairov, V. Raynal, F. Tirode, T. G. P. Grünewald, M. Bohec, S. Baulande, I. Janoueix-Lerosey, J.-P. Vert, E. Barillot, O. Delattre, A. Zinovyev, Transcriptional programs define intratumoral heterogeneity of Ewing sarcoma at single-cell resolution. *Cell Rep.* **30**, 1767–1779.e6 (2020).
40. G.-A. Franzetti, K. Laud-Duval, W. van der Ent, A. Brisac, M. Irondelle, S. Aubert, U. Dirksen, C. Bouvier, G. de Pinieux, E. Snaar-Jagalska, P. Chavrier, O. Delattre, Cell-to-cell

heterogeneity of EWSR1-FLI1 activity determines proliferation/migration choices in Ewing sarcoma cells. *Oncogene* **36**, 3505–3514 (2017).
41. K. Labun, T. G. Montague, M. Krause, Y. N. Torres Cleuren, H. Tjeldnes, E. Valen, CHOPCHOP v3: Expanding the CRISPR web toolbox beyond genome editing. *Nucleic Acids Res.* **47**, W171–W174 (2019).
42. T. Keskin, A. Bakaric, P. Waszyk, G. Boulay, M. Torsello, S. Cornaz-Buros, N. Chevalier, T. Geiser, P. Martin, A. Volorio, S. Iyer, A. Kulkarni, I. Letovanec, S. Cherix, G. M. Cote, E. Choy, A. Digklia, M. Montemurro, I. Chebib, P. G. Nielsen, A. M. Carcaboso, J. Mora, R. Renella, M. L. Suvà, C. Fusco, P. Provero, M. N. Rivera, N. Riggi, I. Stamenkovic, LIN28B underlies the pathogenesis of a subclass of Ewing sarcoma. *Cell Rep.* **31**, 107539 (2020).
43. K. Scotlandi, D. Remondini, G. Castellani, M. C. Manara, F. Nardi, L. Cantiani, M. Francesconi, M. Mercuri, A. M. Caccuri, M. Serra, S. Knuutila, P. Picci, Overcoming resistance to conventional drugs in Ewing sarcoma and identification of molecular predictors of outcome. *J. Clin. Oncol.* **27**, 2209–2216 (2009).
44. S. Postel-Vinay, A. S. Véron, F. Tirode, G. Pierron, S. Reynaud, H. Kovar, O. Oberlin, E. Lapouble, S. Ballet, C. Lucchesi, U. Kontny, A. González-Neira, P. Picci, J. Alonso, A. Patino-Garcia, B. B. de Paillerets, K. Laud, C. Dina, P. Froguel, F. Clavel-Chapelon, F. Doz, J. Michon, S. J. Chanock, G. Thomas, D. G. Cox, O. Delattre, Common variants near TARDBP and EGR2 are associated with susceptibility to Ewing sarcoma. *Nat. Genet.* **44**, 323–327 (2012).
45. S. Savola, A. Klami, S. Myllykangas, C. Manara, K. Scotlandi, P. Picci, S. Knuutila, J. Vakkila, High expression of complement component 5 (*C5*) at tumor site associates with superior survival in Ewing's sarcoma family of tumour patients. *ISRN Oncol.* **2011**, 168712 (2011).
46. S. L. Volchenboum, J. Andrade, L. Huang, D. A. Barkauskas, M. Krailo, R. B. Womer, A. Ranft, J. Potratz, U. Dirksen, T. J. Triche, E. R. Lawlor, Gene expression profiling of Ewing sarcoma tumors reveals the prognostic importance of tumor-stromal interactions: A report from the Children's Oncology Group. *J. Pathol. Clin. Res.* **1**, 83–94 (2015).
47. S. R. Piccolo, Y. Sun, J. D. Campbell, M. E. Lenburg, A. H. Bild, W. E. Johnson, A single-sample microarray normalization method to facilitate personalized-medicine workflows. *Genomics* **100**, 337–344 (2012).
48. Y. Liao, G. K. Smyth, W. Shi, The R package Rsubread is easier, faster, cheaper and better for alignment and quantification of RNA sequencing reads. *Nucleic Acids Res.* **47**, e47 (2019).
49. M. I. Love, W. Huber, S. Anders, Moderated estimation of fold change and dispersion for RNA-seq data with DESeq2. *Genome Biol.* **15**, 550 (2014).

Acknowledgments: We thank A.-C. Clerc of the Cardiovascular Assessment Facility for ultrasonography analysis, and the Cellular Imaging, Flow Cytometry, Mouse Pathology and Animal Facilities of UNIL, as well as the UNIGE IGE3 genomic platform for their support. **Funding:** This work was supported by Swiss National Science Foundation grant 310030-169563 (to I.S.), FNS Sinergia grant CRSII5-177266 (to I.S.), Swiss Cancer League grant KLS-4249-08-2017-R (to I.S.), Swiss National Science Foundation Professorship grant PP00P3-157468/1 (to N.R.), Swiss National Science Foundation Professorship grant PP00P3_183724 (to N.R.), Swiss Cancer League grant KFS-3973-08-2016 (to N.R.), Swiss Cancer League grant KFS4859-08-2019 (to N.R.), the Fond'Action Contre le Cancer Foundation (to N.R.), the FORCE Foundation (to N.R.), the Fondation Emma Muschamp (to N.R.), and National Science Foundation Graduate Research Fellowship DGE1745303 (to E.M.P.). **Author contributions:** Conception and design: C.F., N.R., and I.S. Investigation and methodology: T.K., S.C.-B., B.R., L.B., and P.M. Data analysis: T.K., K.C., E.M.P., P.P., and N.R. Visualization: T.K. and P.P. Resources: I.L., S.L.R., S.C., M.D., R.R., M.L.S., N.R., and I.S. Writing, review, and editing: T.K., N.R., and I.S. Study supervision: C.F., N.R., and I.S. Funding acquisition: N.R. and I.S. **Competing interests:** The authors declare that they have no competing interests. **Data and materials availability:** All data needed to evaluate the conclusions in the paper are present in the paper and/or the Supplementary Materials. Gene expression data generated in this project are available for the Gene Expression Omnibus repository under accession number GSE163699.

Submitted 30 November 2020
Accepted 21 May 2021
Published 2 July 2021
10.1126/sciadv.abf9394

Citation: T. Keskin, B. Rucci, S. Cornaz-Buros, P. Martin, C. Fusco, L. Broye, K. Cisarova, E. M. Perez, I. Letovanec, S. La Rosa, S. Cherix, M. Diezi, R. Renella, P. Provero, M. L. Suvà, I. Stamenkovic, N. Riggi, A live single-cell reporter assay links intratumor heterogeneity to metastatic proclivity in Ewing sarcoma. *Sci. Adv.* **7**, eabf9394 (2021).

A live single-cell reporter assay links intratumor heterogeneity to metastatic proclivity in Ewing sarcoma

Tugba Keskin, Beatrice Rucci, Sandrine Cornaz-Buros, Patricia Martin, Carlo Fusco, Liliane Broye, Katarina Cisarova, Elizabeth M. Perez, Igor Letovanec, Stefano La Rosa, Stephane Cherix, Manuel Diezi, Raffaele Renella, Paolo Provero, Mario L. Suvà, Ivan Stamenkovic and Nicolò Riggi

Sci Adv **7** (27), eabf9394.
DOI: 10.1126/sciadv.abf9394